An arbitrary order variationally consistent integration for Galerkin meshfree methods

Jiun-Shyan Chen*,†, Michael Hillman and Marcus Rüter

Department of Civil and Environmental Engineering, University of California, Los Angeles, CA 90095, USA

SUMMARY

Because most approximation functions employed in meshfree methods are rational functions with overlapping supports, sufficiently accurate domain integration becomes costly, whereas insufficient accuracy in the domain integration leads to suboptimal convergence. In this paper, we show that it is possible to achieve optimal convergence by enforcing variational consistency between the domain integration and the test functions, and optimal convergence can be achieved with much less computational cost than using higher-order quadrature rules. In fact, stabilized conforming nodal integration is variationally consistent, whereas Gauss integration and nodal integration are not. In this work the consistency conditions for arbitrary order exactness in the Galerkin approximation are set forth explicitly. The test functions are then constructed to be variationally consistent with the integration scheme up to a desired order. Attempts are also made to correct methods that are variationally inconsistent via modification of test functions, and several variationally consistent methods are derived under a unified framework. It is demonstrated that the solution errors of PDEs due to quadrature inaccuracy can be significantly reduced when the variationally inconsistent methods are corrected with the proposed method, and consequently the optimal convergence rate can be either partially or fully restored. Copyright © 2013 John Wiley & Sons, Ltd.

1. INTRODUCTION

In recent decades, meshfree methods have become of growing interest due to the applicability of the method to classes of problems that present difficulty in traditional mesh-based methods. Examples include large deformation problems such as metal forming processes [1], moving discontinuities in fracture mechanics [2, 3], penetration processes [4], and earth moving simulations [5], among others. Although significant progress in meshfree methods has been made over the years, issues in domain integration remain to be addressed.

In meshfree methods, the shape functions are typically rational, and their supports overlap. Therefore it is difficult to develop accurate and efficient numerical integration for these methods. Roughly speaking, this results in two major issues in meshfree methods with inappropriate domain integration: the deterioration of accuracy and convergence rates, and a spatial instability in some node-based integration techniques.

In early literature [6, 7], background cells were used for Gauss integration and no special treatment was taken to alleviate the problems associated with integration. Dolbow and Belytschko [8] first investigated the integration issue in the element-free Galerkin method and showed that although moving least squares (MLS) shape functions are rational and thus more difficult to integrate, the

---

*Correspondence to: Jiun-Shyan Chen, Department of Civil and Environmental Engineering, University of California, Los Angeles, CA 90095, USA.

†E-mail: jschen@seas.ucla.edu

main source of error in domain integration with Gauss quadrature is the misalignment of shape function supports with integration cells. They proposed an integration scheme where supports and integration cells are aligned for enhanced accuracy and convergence. Various other methods have been proposed to address integration in meshfree methods. The meshless local Petrov–Galerkin method [9] uses the local weak form such that the support of each shape function can be used as integration cells with proper quadrature rules for the local integration domain. A similar technique has been used in the method of finite spheres, as introduced in [10, 11]. However, these methods are expensive, as many integration points are repeatedly evaluated. More recently, Liu and Belytschko [12] devised a method on the basis of this idea, combined with satisfaction of the linear patch test. Methods based on the partition of unity have also been proposed [13, 14] to construct a method that is free of background integration cells. In these methods, the domain integration is separated into a series of integrands that cover the domain, each weighted by the partition of unity function.

If nodal integration is employed for domain integration to maintain the meshfree character of the method, a well-known spatial instability arises [15, 16]. This is because first derivatives of shape functions are zero or nearly zero at nodes, resulting in spurious modes from underestimating the energy associated with small (two times the nodal spacing) wavelength modes. In this situation, modes of alternating nodal displacements are left virtually unchecked as their contribution to the bilinear form is small. Beissel and Belytschko [15] introduced a least squares residual-based method where the second-order derivatives stabilize the rank instability. The approach eliminates the oscillatory behavior but at the cost of increasing the completeness of the basis functions to quadratic, and thus requiring a larger support and further increasing computational cost. Chen *et al*. [16] introduced a stabilized conforming nodal integration method (SCNI) that uses strain smoothing to achieve Galerkin linear exactness and to take derivatives away from the nodes to circumvent rank instability. More recently, it has been shown that SCNI generates nonzero low energy modes because of the loss of coercivity in the limit of discretization, and a correction has been proposed to enhance the stability [17, 18]. The SCNI approach has also been introduced as a nodal integration technique in finite elements [19]. Stress point methods have also been proposed [20] for SPH where derivatives are taken away from the nodes so that the spurious modes are not present.

To address the error induced by quadrature, a model problem of interest has been the patch test. The conditions on the domain and boundary integration for passing the linear patch test as to yield linear exactness in the Galerkin approximation have been investigated in [16, 21, 22] and were termed integration constraints [16]. Several corrections based on these conditions have been proposed. Bonet and Kulasegaram [22] have arrived at the condition for SPH, and a correction of the bilinear form was proposed based on the satisfaction of the integration constraints which involved an iterative procedure. Chen *et al*. [16] derived the integration constraint by enforcing linear exactness in the Galerkin approximation with quadrature and proposed SCNI where the strains are smoothed with divergence operation on a set of conforming subdomains such that the integration constraint is satisfied. SCNI has been applied to various problems such as plate and shell problems [23–25], where an integration constraint to achieve bending exactness so as to avoid shear locking has been derived, and a strain smoothing on the curvature has been proposed. This approach was further extended by Wang and Chen [25] to introduce a subdomain stabilized conforming integration to achieve a locking free solution while maintaining spatial stability. Duan *et al*. [26] extended the linear exactness of SCNI to quadratic exactness by solving for the shape function derivatives at each integration point. Similar to SCNI, conforming integration cells are adapted to meet integration constraints. Error analysis of quadrature in meshfree methods has been carried out in [27, 28], where a zero row-sum condition for improving convergence behavior has been introduced, and a correction on diagonal terms of the stiffness matrix to achieve the zero row-sum condition has been proposed.

In this work, we focus on obtaining the requirements in domain integration to achieve arbitrary order exactness in the Galerkin meshfree methods as an extension of linear integration constraints [16] to higher-order constraints. Assuming the nth order completeness of the trial functions is attained, close examination reveals that the conditions for n^{th} order exactness are related to both the integration scheme and the choice of test functions. These conditions state that using the chosen numerical integration, integration by parts holds for the inner product of the test functions and the differential operator acting on the nth order monomials. The domain integration methods that

meet these conditions are referred to as variationally consistent integration (VCI) methods herein. By using this as a basis, we construct a set of test functions consistent with the integration scheme for satisfaction of the integration constraints. The method allows for arbitrarily high order exactness for arbitrary types of integration methods, and it is demonstrated numerically that convergence rates predicted by exact integration are either partially or fully restored, and the integration error is significantly reduced when the integration constraints are met.

The outline of the paper is as follows. Section 2 gives a basic overview of domain integration for Galerkin meshfree methods, and demonstrates that some commonly used numerical integration methods can severely deteriorate accuracy and convergence. In Section 3 the integration constraints for n^{th} order exactness are derived and applied to several BVPs. Section 4 introduces ways to construct test functions consistent with the integration scheme and proposes an assumed strain method to satisfy the nth order integration constraints. Section 5 discusses the stability of the proposed method for meeting integration constraints. In Section 6, the method is applied to several problems demonstrating improved error and convergence over standard methods. Finally, concluding remarks are given in Section 7.

2. BACKGROUND

In this section, we identify the issues in the domain integration of Galerkin meshfree methods. We show how several commonly used domain integration methods such as nodal integration and Gauss integration exhibit suboptimal convergence behavior under certain discretizations. The reproducing kernel particle method (RKPM) will be used to demonstrate the integration issues, but the same applies to other Galerkin meshfree methods. The discussions in this section serve as the motivation of the present work.

2.1. Reproducing kernel approximation

We consider the reproducing kernel (RK) approximation herein to demonstrate the nature of approximation functions commonly used in meshfree methods. Let the closed domain $\bar{\Omega} \subset \mathbb{R}^d$ with dimension d be discretized by a set of NP nodes $\{x_I | x_I \in \bar{\Omega}\}_{I=1}^{NP}$. The RK approximation of a function $u(x)$ in $\bar{\Omega}$ denoted by $u^h(x)$ is constructed by the product of a kernel function $\Phi_a(x - x_I)$ with compact support and a correction function composed of a linear combination of basis functions in the following form [29]:

$$u^h(x) = \sum_{I=1}^{NP} \left\{ \sum_{|\alpha| \leqslant n} (x - x_I)^\alpha b_\alpha(x) \right\} \Phi_a(x - x_I) u_I \equiv \sum_{I=1}^{NP} \Psi_I(x) u_I. \tag{1}$$

Here we have introduced the multi-index notation $\alpha = (\alpha_1, \alpha_2, \ldots, \alpha_d)$ with the length of α defined as $|\alpha| = \sum_{i=1}^d \alpha_i$, $x^\alpha \equiv x_1^{\alpha_1} \cdot x_2^{\alpha_2} \cdot \ldots \cdot x_d^{\alpha_d}$, $x_I^\alpha \equiv x_{I1}^{\alpha_1} \cdot x_{I2}^{\alpha_2} \cdot \ldots \cdot x_{Id}^{\alpha_d}$, $b_\alpha = b_{\alpha_1 \alpha_2 \cdots \alpha_d}$, and u_I are the coefficients of approximation. The term $\{(x - x_I)^\alpha\}_{|\alpha| \leqslant n}$ is the set of basis functions, and $\{b_\alpha(x)\}_{|\alpha| \leqslant n}$ are coefficients that are determined by meeting the reproducing conditions

$$\sum_{I=1}^{NP} \Psi_I(x) x_I^\alpha = x^\alpha, \quad |\alpha| \leqslant n. \tag{2}$$

With $\{b_\alpha(x)\}_{|\alpha| \leqslant n}$ obtained from (2), the RK shape functions are obtained as

$$u^h(x) = \sum_{I=1}^{NP} \Psi_I(x) u_I \tag{3}$$

where

$$\Psi_I(x) = H(0)^T M^{-1}(x) H(x - x_I) \Phi_a(x - x_I) \tag{4}$$

$$M(x) = \sum_{I=1}^{NP} H(x - x_I) H^T(x - x_I) \Phi_a(x - x_I). \tag{5}$$

Here, the vector $H^T(x - x_I)$ is the corresponding row vector of $\{(x - x_I)^\alpha\}_{|\alpha| \leqslant n}$ and $M(x)$ is the moment matrix. In this construction, the reproducing conditions (2) are met provided the moment matrix (5) is invertible, and this requires sufficient nodes under the cover of Φ_a so that the reproducing equations are linearly independent [30]. By direct differentiation, the shape functions also satisfy the gradient property

$$\sum_{I=1}^{NP} \nabla \Psi_I(x) x_I^\alpha = \nabla x^\alpha, \quad |\alpha| \leqslant n. \tag{6}$$

The gradient completeness in (6) is one of the necessary conditions to pass the patch test. It is important to note that meshfree shape functions such as the RK shape functions in (3) can be rational functions, and the shape function supports are often overlapping. This adds complexity to domain integration in meshfree methods.

2.2. Issues in domain integration

When shape functions are rational such as the RK shape functions in (3), exact domain integration may not be possible. Exactness in the Galerkin approximation is not guaranteed even if the test functions possess sufficient completeness to represent the solution. As shown in [16], the exactness in the Galerkin approximation is guaranteed provided additional integration constraints are met. For first order Galerkin exactness, the linear integration constraint is the condition to numerically integrate the divergence equality [16]:

$$\langle \nabla \Psi_I \rangle_\Omega = \langle \Psi_I n \rangle_{\partial\Omega} \quad \forall I, \tag{7}$$

where $\langle \cdot \rangle_\Omega = \hat{\int}_\Omega \cdot \, d\Omega$ and $\langle \cdot \rangle_{\partial\Omega} = \hat{\int}_{\partial\Omega} \cdot \, d\Gamma$ denote numerical versions of domain and boundary integrals, respectively, with '$\hat{}$' denoting numerical integration, and Ψ_I is a shape function with first-order completeness used in the Galerkin equation. Passing the patch tests (Galerkin exactness) for meshfree methods is in general not straightforward. Even high order Gauss integration (GI) is in general unable to meet the integration constraint, and therefore it cannot provide Galerkin exactness in meshfree methods. Methods such as stabilized conforming nodal integration [16, 23, 24, 31, 32] have been proposed that are specifically formulated to meet the integration constraints and therefore pass the associated patch tests.

Let us examine the effect of various conventional domain integration techniques on the accuracy of Galerkin meshfree methods. The patch test requires that the exact solution of a certain order be obtained for the BVP at hand. If the shape functions possess sufficient completeness, then this is achievable provided the additional integration constraints are met.

As an example, consider a linear patch test for the Poisson equation:

$$\nabla^2 u + s = 0 \quad \text{in } \Omega \tag{8a}$$

$$\nabla u \cdot n = h \quad \text{on } \partial\Omega_h \tag{8b}$$

$$u = g \quad \text{on } \partial\Omega_g, \tag{8c}$$

where $\Omega : (-1, 1) \times (-1, 1)$, $\partial\Omega_h : -1 \leqslant x \leqslant 1, y = 1$, $\partial\Omega_g = \partial\Omega \setminus \partial\Omega_h$. Let the prescribed conditions to (8) be

$$s = 0 \tag{9a}$$

$$h = n_1 + 2n_2 \tag{9b}$$

$$g = x + 2y. \tag{9c}$$

The solution to the BVP (8) with conditions (9) is $u = x + 2y$.

The domain Ω is discretized with uniform and nonuniform node distributions. For the generation of the nonuniform discretization, a perturbation parameter β is introduced to perturb the nodes away from a uniform distribution with spacing Δx_i by $x_{iI} = x_{iI}^0 + \eta_{Ii} \Delta x_i$, $-\beta \leqslant \eta_{Ii} \leqslant \beta$, where x_{iI}^0 is the uniform nodal position, x_{iI} is the perturbed node position, and η_{Ii} is generated randomly for each node in each direction. In nonuniform node distributions, the integration constraint tends to be violated more because of the asymmetry of the location of the integration points with respect to nodes and the asymmetry of the shape functions themselves. Figure 1 shows the domain discretizations used with integration schemes for GI and direct nodal integration (DNI).

Because both Gauss integration and direct nodal integration fail to meet the linear integration constraint, they fail the patch test as seen in Table I. Although linear bases are used, meeting the linear completeness requirement alone is not sufficient for passing linear patch test. DNI performs poorly, whereas GI is seen to provide better results as the number of integration points increases. However, when the number of Gauss points is increased from 1×1 to 5×5, the error still remains. Although the patch test can be 'nearly' passed for high order integration, the cost increase can be significant. Here, it is seen that for $\beta = 1$, the error is reduced by an order of magnitude from 1×1 GI to 3×3 GI and an additional order from 3×3 to 5×5 GI. Lastly, it can be seen that for irregular node distributions, the error can be several orders of magnitude larger than in the uniform case.
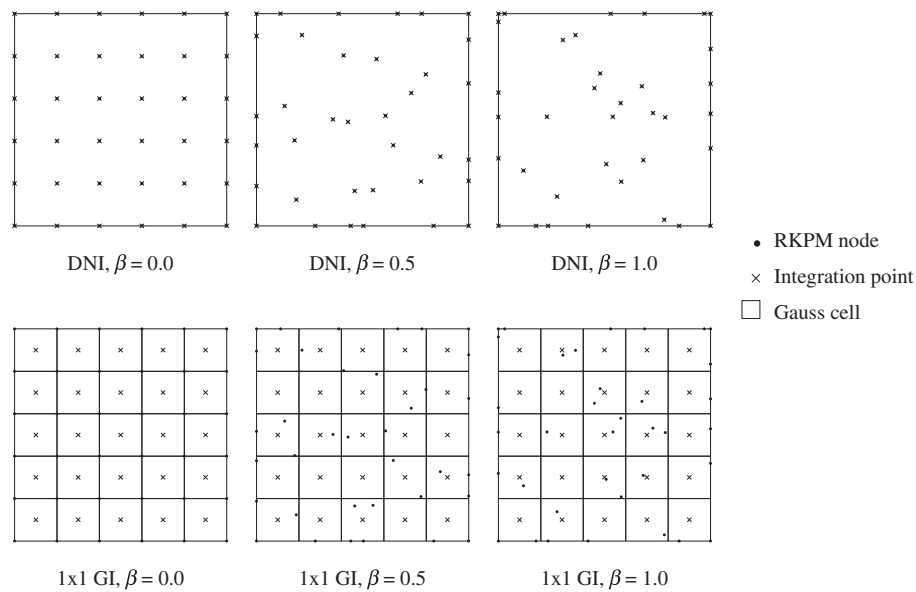

Figure 1. Integration schemes for direct nodal integration (DNI) and 1×1 Gauss integration (GI) for uniform and nonuniform node distributions.

Table I. L^2 norm of error for various integration methods.

Method	β		
	0.0	0.5	1.0
DNI	0.0236688	0.7213156	0.6750119
1×1 GI	0.0071572	0.3163669	1.6402035
2×2 GI	0.0001916	0.0649164	0.0782014
3×3 GI	0.0000333	0.0115104	0.0241756
4×4 GI	0.0000087	0.0053343	0.0066763
5×5 GI	0.0000013	0.0015578	0.0019404

DNI, direct nodal integration; GI, Gauss integration.

Under integration can result in suboptimal convergence. To demonstrate this, consider a convergence study for the same BVP (8) with the source term and pure essential boundary condition:

$$s = \sin(\pi x) \sin(\pi y) \tag{10a}$$

$$g = 0. \tag{10b}$$

Here, the entire boundary is subjected to $g = 0$. The exact solution of this problem is

$$u = \frac{1}{2\pi^2} \sin(\pi x) \sin(\pi y). \tag{11}$$

First, the domain is discretized uniformly with 36, 121, 441, and 1681 nodes, and an RK approximation with linear bases and a normalized support of 1.75 is employed. In this case, the integration constraint is met for nodes with kernel functions that do not cover the boundary of the domain, because GI and direct integration points are symmetric with respect to the shape functions. Consequently, as seen in Figure 2 (numbers in the legends indicate rates of convergence), the convergence behavior is optimal. It is noted here that the H^1 semi-norm turns into the energy norm for this particular problem.
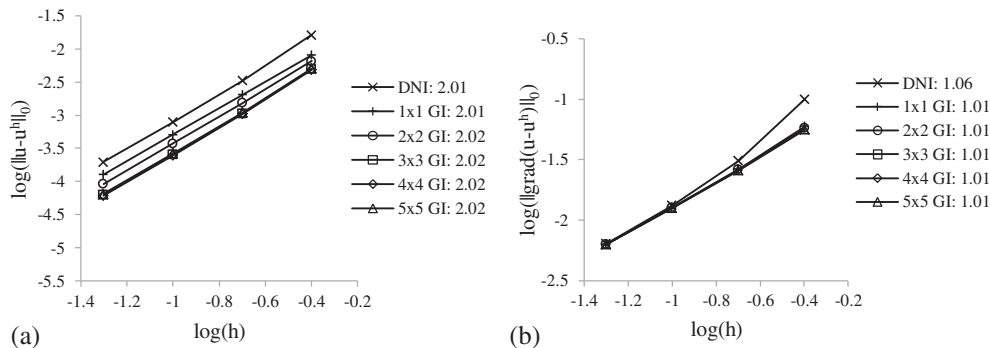

Figure 2. Convergence of error in (a) the L^2 norm and (b) the H^1 semi-norm for uniform discretization for Gauss integration (GI) and direct nodal integration (DNI).
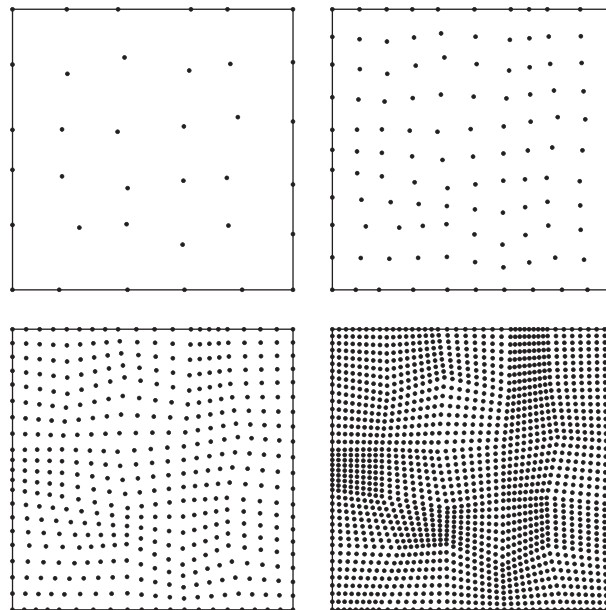

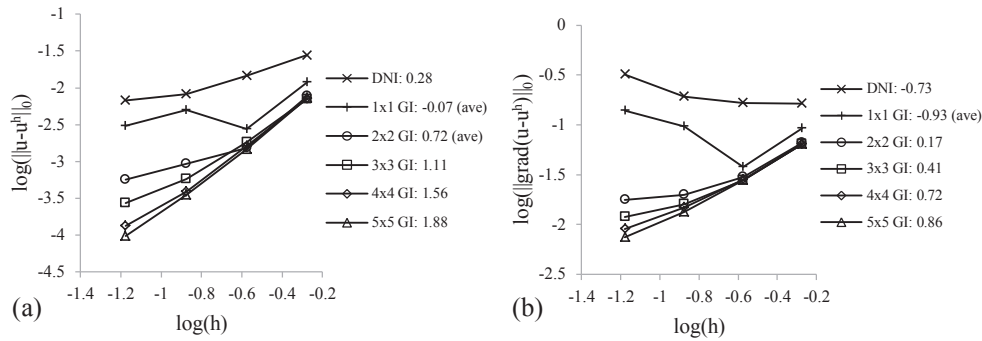Figure 3. Uniform refinement of irregular node distribution.

Figure 4. Convergence of error in (a) the L^2 norm and (b) the H^1 semi-norm for nonuniform discretization for Gauss integration (GI) and direct nodal integration (DNI).

The domain is then discretized with a nonuniform node distribution with the random generation parameter $\beta = 0.2$ in the coarse discretization and refined uniformly as shown in Figure 3. Herein, the characteristic length for convergence h is taken as the maximum nodal spacing for the first discretization and halved for each subsequent discretization.

Direct nodal integration and GI are again employed; the error in the L^2 norm and H^1 semi-norm are shown in Figure 4. In nonuniform convergence studies, when the convergence is erratic, the average rate is taken as indicated in the figure. It can be seen that although the shape functions possess linear completeness, the optimal convergence rates of 2 in the L^2 norm and 1 in the H^1 semi-norm are not obtained, and can in fact be much lower than these optimal rates. The two methods of simple integration (1×1 GI and DNI) behave erratically with respect to the convergence and accuracy, as it is seen that the H^1 semi-norm of the error actually diverges with refinement. It is also seen that the convergence rate can be partially restored, but even with 5×5 GI, the rate is not full in the H^1 semi-norm.

2.3. Stabilized conforming and nonconforming nodal integration

Stabilized conforming nodal integration has been introduced [16] to meet the linear integration constraint (7) and to remedy rank instability in DNI. In this method, gradients are smoothed over conforming cells that partition the domain as shown in Figure 5(a). The cells can be generated by using Voronoi diagrams or Delaunay triangulations. SCNI considers gradient smoothing with divergence in each nodal representative domain by

$$\tilde{\nabla} u^h(\boldsymbol{x}_L) = \frac{1}{A_L} \int_{\Omega_L} \nabla u^h(\boldsymbol{x}) \, d\Omega = \frac{1}{A_L} \int_{\partial\Omega_L} u^h(\boldsymbol{x}) \boldsymbol{n}(\boldsymbol{x}) \, d\Gamma. \tag{12}$$

Here $A_L = \int_{\Omega_L} d\Omega$ and Ω_L is the representative domain of node L.
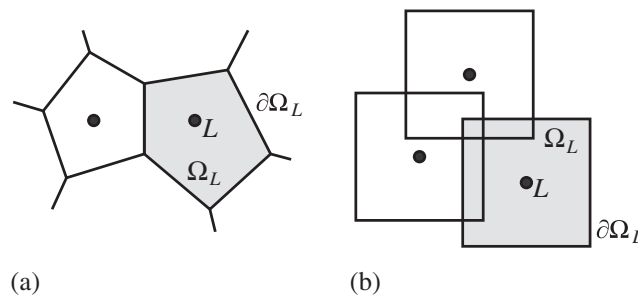

Figure 5. Nodal representative domain (a) by Voronoi diagram for stabilized conforming nodal integration (b) for stabilized nonconforming nodal integration smoothing scheme.

With (3), the approximation of the gradient at each node can be expressed in terms of the averaged (smoothed) shape function gradient

$$\tilde{\nabla} u^h(\boldsymbol{x}_L) = \sum_{I=1}^{NP} \tilde{\nabla} \Psi_I(\boldsymbol{x}_L) u_I, \tag{13}$$

where

$$\tilde{\nabla} \Psi_I(\boldsymbol{x}_L) = \frac{1}{A_L} \int_{\partial \Omega_L} \Psi_I(\boldsymbol{x}) \boldsymbol{n}(\boldsymbol{x}) \, d\Gamma. \tag{14}$$

If numerical integration is employed, (14) is expressed as

$$\tilde{\nabla} \Psi_I(\boldsymbol{x}_L) = \frac{1}{A_L} \langle \Psi_I \boldsymbol{n} \rangle_{\partial \Omega_L}. \tag{15}$$

It is easily shown that nodal integration with the smoothed gradient in (15) meets the integration constraint (7) if the smoothing domains $\{\Omega_L\}_{L=1}^{NINT}$ are conforming [16]:

$$\langle \tilde{\nabla} \Psi_I \rangle_\Omega = \sum_{L=1}^{NINT} \tilde{\nabla} \Psi_I(\boldsymbol{x}_L) A_L = \sum_{L=1}^{NINT} \langle \Psi_I \boldsymbol{n} \rangle_{\partial \Omega_L} = \langle \Psi_I \boldsymbol{n} \rangle_{\partial \Omega}, \tag{16}$$

where $NINT$ is the number of integration points. To yield linear exactness in the Galerkin approximation of second-order PDEs by using SCNI, the boundary integration rules used in $\langle \Psi_I \boldsymbol{n} \rangle_{\partial \Omega_L}$ in (15) should be used for natural or essential boundary terms in the weak form as can be understood from (7) and the Galerkin weak form of (8).

The formation of conforming strain smoothing domains in SCNI can be cumbersome in problems subjected to topological change in geometry, and stabilized nonconforming nodal integration (SNNI) has been introduced [4,5] as a simplification of SCNI. Figure 5(b) depicts a typical smoothing scheme for SNNI where the smoothing zones are nonconforming. For illustration, SCNI and SNNI are employed for solving the patch test problem described by (8) and (9). Figure 6 shows the gradient smoothing schemes by conforming Voronoi cells and nonconforming cells for the discretizations. The integration weights used in both methods are the nodal areas in the Voronoi diagram.
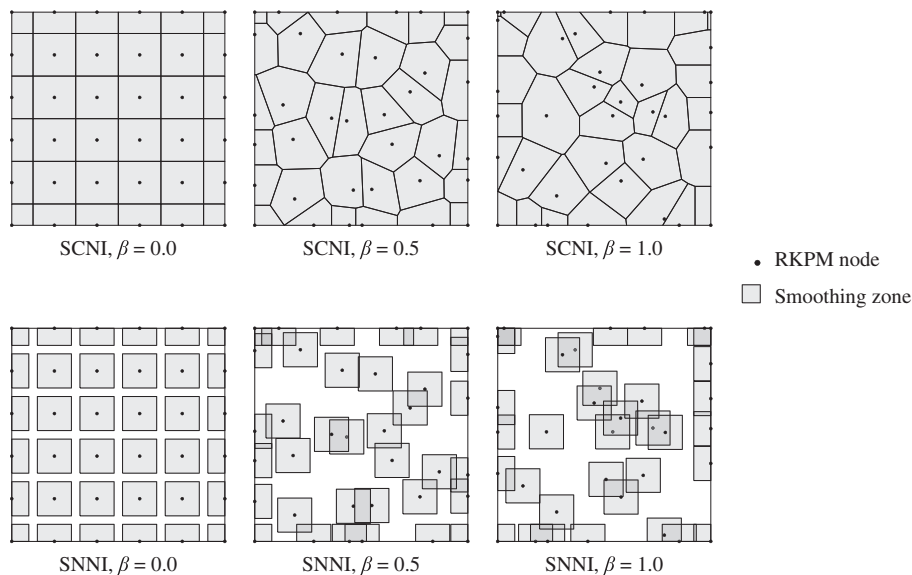

Figure 6. Gradient smoothing domains in smoothed nodal integration methods.

Table II. L^2 norm of error for smoothed integration methods.

Method	β		
	0.0	0.5	1.0
SCNI	1.34E-15	3.51E-14	1.06E-14
SNNI	0.0259761	0.4509896	0.9459201

SCNI, stabilized conforming nodal integration; SNNI, stabilized nonconforming nodal integration.
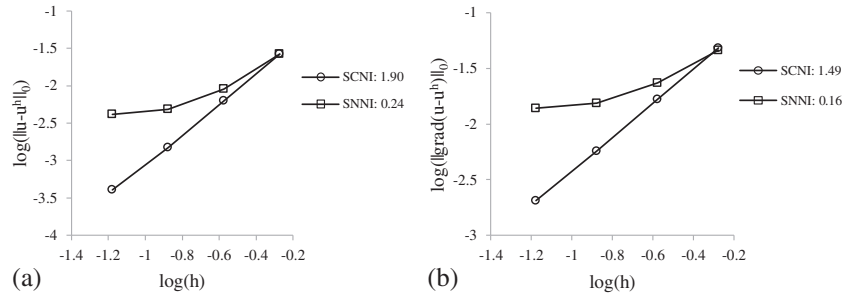

Figure 7. Convergence of error in (a) the L^2 norm and (b) the H^1 semi-norm for nonuniform discretization for stabilized conforming nodal integration (SCNI) and stabilized nonconforming nodal integration (SNNI).

Table II shows the error of patch test by using nodal integration with the two gradient smoothing methods. For SCNI, the result passes the patch test to machine precision, whereas SNNI does not pass the patch test. The consequence of passing or violating patch test can be demonstrated in the convergence test described by Equations (8) and (10), with the nonuniform discretizations shown in Figure 3. The L^2 norm and H^1 semi-norm of the errors are plotted in Figure 7, showing that SCNI provides optimal convergence in the L^2 norm and in derivatives, whereas SNNI converges at a much lower rate in the L^2 norm and in the H^1 semi-norm. It is noted that, similar to the cases of DNI and GI, optimal convergence can be obtained when a uniform discretization is employed.

Remarks 2.1

(1) To satisfy linear completeness, which is the first requirement to meet Galerkin exactness, it is sufficient to take single point integration on each boundary face in the smoothed methods so that

$$\langle \boldsymbol{n} \rangle_{\partial \Omega_L} = \langle \nabla 1 \rangle_{\Omega_L} \tag{17a}$$

$$\langle \boldsymbol{n} x \rangle_{\partial \Omega_L} = \langle \nabla x \rangle_{\Omega_L} \tag{17b}$$

$$\langle \boldsymbol{n} y \rangle_{\partial \Omega_L} = \langle \nabla y \rangle_{\Omega_L}. \tag{17c}$$

Using (17a), the smoothed gradients meet the gradient partition of nullity

$$\sum_{I=1}^{NP} \tilde{\nabla} \Psi_I(\boldsymbol{x}_L) = \frac{1}{A_L} \left\langle \left(\sum_{I=1}^{NP} \Psi_I \right) \boldsymbol{n} \right\rangle_{\partial \Omega_L} = \frac{1}{A_L} \langle \boldsymbol{n} \rangle_{\partial \Omega_L} = \boldsymbol{0}. \tag{18}$$

Similarly, the smoothed gradients meet the first-order gradient reproducing condition by using (17b) and (17c) and if the approximation is first-order complete

$$\sum_{I=1}^{NP} \tilde{\nabla} \Psi_I x_I(\boldsymbol{x}_L) = \frac{1}{A_L} \left\langle \left(\sum_{I=1}^{NP} \Psi_I x_I \right) \boldsymbol{n} \right\rangle_{\partial \Omega_L} = \frac{1}{A_L} \langle \boldsymbol{n} x \rangle_{\partial \Omega_L} = \left\{ \begin{array}{c} 1 \\ 0 \end{array} \right\} \tag{19a}$$

and

$$\sum_{I=1}^{NP} \tilde{\nabla}\Psi_I y_I(\boldsymbol{x}_L) = \frac{1}{A_L}\left\langle \left(\sum_{I=1}^{NP}\Psi_I y_I\right)\boldsymbol{n}\right\rangle_{\partial\Omega_L} = \frac{1}{A_L}\langle\boldsymbol{n}y\rangle_{\partial\Omega_L} = \begin{Bmatrix} 0 \\ 1 \end{Bmatrix}. \tag{19b}$$

(2) For smoothed integration methods, an additional condition analogous to (17) is required to meet quadratic gradient reproducing conditions:

$$\langle\boldsymbol{n}x^2\rangle_{\partial\Omega_L} = \langle\nabla x^2\rangle_{\Omega_L} \tag{20a}$$

$$\langle\boldsymbol{n}y^2\rangle_{\partial\Omega_L} = \langle\nabla y^2\rangle_{\Omega_L} \tag{20b}$$

$$\langle\boldsymbol{n}xy\rangle_{\partial\Omega_L} = \langle\nabla xy\rangle_{\Omega_L}. \tag{20c}$$

Further, let the nodes coincide with the centroid $\boldsymbol{x}_c$ of the smoothing zones defined by

$$x_c = \frac{1}{A_L}\langle x\rangle_{\Omega_L} = \frac{1}{2A_L}\langle x^2 n_1\rangle_{\partial\Omega_L} \tag{21a}$$

$$y_c = \frac{1}{A_L}\langle y\rangle_{\Omega_L} = \frac{1}{2A_L}\langle y^2 n_2\rangle_{\partial\Omega_L}. \tag{21b}$$

Here, (20) has been used to result in (21). By using (20) and (21), the second-order gradient reproducing conditions are satisfied at each nodal position $\boldsymbol{x}_c$ by

$$\sum_{I=1}^{NP} \tilde{\nabla}\Psi_I x_I^2(\boldsymbol{x}_c) = \frac{1}{A_L}\langle\boldsymbol{n}x^2\rangle_{\partial\Omega_L} = \begin{Bmatrix} 2x_c \\ 0 \end{Bmatrix} \tag{22a}$$

$$\sum_{I=1}^{NP} \tilde{\nabla}\Psi_I y_I^2(\boldsymbol{x}_c) = \frac{1}{A_L}\langle\boldsymbol{n}y^2\rangle_{\partial\Omega_L} = \begin{Bmatrix} 0 \\ 2y_c \end{Bmatrix} \tag{22b}$$

$$\sum_{I=1}^{NP} \tilde{\nabla}\Psi_I x_I y_I(\boldsymbol{x}_c) = \frac{1}{A_L}\langle\boldsymbol{n}xy\rangle_{\partial\Omega_L} = \begin{Bmatrix} y_c \\ x_c \end{Bmatrix}. \tag{22c}$$

In two dimensions, the above relationships can be satisfied by using the two-point GI for each boundary segment of arbitrary polygon smoothing zones and single point integration for each boundary segment of square smoothing zones, provided the nodal location is at $\boldsymbol{x}_c$ for both cases.

3. VARIATIONALLY CONSISTENT INTEGRATION FOR HIGH ORDER EXACTNESS IN THE GALERKIN APPROXIMATION

In this section, we demonstrate how arbitrary order exactness in the Galerkin approximation can be achieved if the test function and domain integration are variationally consistent. This concept is a generalization of the integration constraint for first-order Galerkin exactness for the second-order PDE as introduced in [16]. These constraint conditions serve as the basis for deriving variationally consistent domain integrations to be discussed in Section 4.

3.1. Model problem

Here, the integration constraint for linear exactness in the Galerkin approximation of second-order PDEs (7) is generalized to high order solutions and general PDEs. Consider the following abstract boundary value problem:

$$Lu + s = 0 \quad \text{in } \Omega \tag{23a}$$

$$Bu = h \quad \text{on } \partial\Omega_h \tag{23b}$$

$$u = g \quad \text{on } \partial\Omega_g. \tag{23c}$$

In the above, L is a differential operator acting in the domain $\Omega \subset \mathbb{R}^d$, s is a source term, g is the prescribed values of u on the essential boundary $\partial \Omega_g$, B is a boundary operator acting on the natural boundary $\partial \Omega_h$, and the boundary of the domain $\partial \Omega$ admits the decomposition $\partial \Omega_g \cap \partial \Omega_h = \emptyset$ and $\partial \Omega = \partial \Omega_g \cup \partial \Omega_h$.

Although traditionally essential boundary terms are omitted in the weighted residual because of the availability of the kinematically admissible trial space, in meshfree methods this may not be the case and the essential boundary conditions should be imposed as constraints by, for example, Lagrange multiplier methods, Nitsche's method, or the modified variational principle. To keep the formulation general, Lagrange multipliers shall be employed for the enforcement of boundary conditions herein, but what follows applies to all consistent weak forms, that is, all weak forms that attest to the strong form (23).

The weak form of the BVP seeks $(u, \lambda) \in U \times \Lambda$ such that for all $(v, \gamma) \in V \times \Gamma$ the following equation holds:

$$a(v, u)_\Omega = (v, s)_\Omega + (v, h)_{\partial \Omega_h} + (v, \lambda)_{\partial \Omega_g} + (\gamma, u - g)_{\partial \Omega_g}, \tag{24}$$

where U, Λ, V, and Γ are adequate Sobolev spaces associated with the differential operator L. Here $(v, s)_\Omega = \int_\Omega vs \ d\Omega$ denotes the L^2 inner product in Ω, $(v, h)_{\partial \Omega_h} = \int_{\partial \Omega_h} vh \ d\Gamma$ and $(v, \lambda)_{\partial \Omega_g} = \int_{\partial \Omega_g} v\lambda \ d\Gamma$ denote L^2 inner products on the natural and essential boundaries of Ω, respectively, and a is a bilinear form which results from the integration by parts formula $(v, Lu)_\Omega = (v, Bu)_{\partial \Omega} - a(v, u)_\Omega$. Note that using the equivalence of the weak and strong forms, the Lagrange multiplier is obtained as

$$\lambda = Bu \quad \text{on } \partial \Omega_g. \tag{25}$$

Substitution of (25) into (24) gives the modified variational principle [33]. However for illustration, the Lagrange multiplier form shall be used.

3.2. Variational consistency condition: a generalization of the linear integration constraint

Consider the abstract boundary value problem (23) where the solution is complete monomials with degree n:

$$u = \sum_{|\alpha| \leq n} c_\alpha x^\alpha \equiv u^n, \tag{26}$$

where the multi-index notation is that used in (1). The source term and boundary conditions consistent with this solution are

$$s = -Lu^n \quad \text{in } \Omega \tag{27a}$$
$$h = Bu^n \quad \text{on } \partial \Omega_h \tag{27b}$$
$$g = u^n \quad \text{on } \partial \Omega_g. \tag{27c}$$

That is, when the boundary conditions and source term are prescribed as (27), the solution to the BVP of (23) is (26). For this solution the Lagrange multiplier takes the form

$$\lambda^n = Bu^n \quad \text{on } \partial \Omega_g. \tag{28}$$

The Galerkin approximation seeks $(u^h, \lambda^h) \in U^h \times \Lambda^h$ such that for all $(v^h, \gamma^h) \in V^h \times \Gamma^h$ the following equation holds:

$$a(v^h, u^h)_\Omega = (v^h, s)_\Omega + (v^h, h)_{\partial \Omega_h} + (v^h, \lambda^h)_{\partial \Omega_g} + (\gamma^h, u^h - g)_{\partial \Omega_g}, \tag{29}$$

where $U^h \subset U$, $V^h \subset V$, $\Lambda^h \subset \Lambda$, and $\Gamma^h \subset \Gamma$ are suitable finite-dimensional subspaces. Let the trial and test functions be approximated as

$$u^h = \sum_{I=1}^{NP} \Psi_I u_I \tag{30a}$$

$$v^h = \sum_{I=1}^{NP} \hat{\Psi}_I v_I \tag{30b}$$

$$\lambda^h = \sum_{I=1}^{NC} \varphi_I \lambda_I \tag{30c}$$

$$\gamma^h = \sum_{I=1}^{NC} \hat{\varphi}_I \gamma_I, \tag{30d}$$

where NC is the number of constraint nodes associated with the essential boundary condition. Note that in the Bubnov–Galerkin method, $\hat{\Psi}_I = \Psi_I$ and $\hat{\varphi}_I = \varphi_I$, and for a Petrov–Galerkin method they are different from each other. Consider the nth order completeness in u^h in (2):

$$\sum_{I=1}^{NP} \Psi_I u_I^n = u^n, \tag{31}$$

where u^n is the complete n^{th} order monomial defined in (26), and $u_I^n = \sum_{|\alpha| \le n} c_\alpha x_I^\alpha$. By using the approximations (30), inserting $u_J = u_J^n$ into the last term in (29), using the essential boundary condition (27c), and the completeness condition (31), we have

$$\sum_{J=1}^{NP} a(\hat{\Psi}_I, \Psi_J u_J)_\Omega = (\hat{\Psi}_I, s)_\Omega + (\hat{\Psi}_I, h)_{\partial\Omega_h} + \sum_{J=1}^{NC} (\hat{\Psi}_I, \varphi_J \lambda_J)_{\partial\Omega_g} \quad \forall I. \tag{32}$$

By taking $\lambda_I = \lambda_I^n = (Bu^n)_I$, inserting $u_J = u_J^n$, and using the completeness condition in the approximation of $\lambda^h = \sum_{I=1}^{NC} \varphi_I \lambda_I^n = \sum_{I=1}^{NC} \varphi_I (Bu^n)_I = Bu^n$ we arrive at

$$\sum_{J=1}^{NP} a(\hat{\Psi}_I, \Psi_J u_J^n)_\Omega = (\hat{\Psi}_I, s)_\Omega + (\hat{\Psi}_I, h)_{\partial\Omega_h} + (\hat{\Psi}_I, Bu^n)_{\partial\Omega_g} \quad \forall I. \tag{33}$$

Finally, by using the source term (27a) and boundary conditions (27b) and (27c), considering all orders of completeness from 1 to n, and employing numerical integration in (33), we have

$$a\langle\hat{\Psi}_I, x^\alpha\rangle_\Omega = -\langle\hat{\Psi}_I, Lx^\alpha\rangle_\Omega + \langle\hat{\Psi}_I, Bx^\alpha\rangle_{\partial\Omega} \quad \forall I, |\alpha| = 0, 1, \ldots, n, \tag{34}$$

where $a\langle\cdot, \cdot\rangle_\Omega$ is the quadrature version of $a(\cdot, \cdot)_\Omega$, and $\langle\cdot, \cdot\rangle_\Omega$ and $\langle\cdot, \cdot\rangle_{\partial\Omega}$ are the quadrature versions of $(\cdot, \cdot)_\Omega$ and $(\cdot, \cdot)_{\partial\Omega}$, respectively. The equations in (34) are a generalization of the linear integration constraints to arbitrary order of Galerkin exactness. Domain integration that meets (34) yields Galerkin exactness with a desired order and is called VCI herein.

Remarks 3.1

(1) To arrive at the nth order integration constraints in (34), n^{th} order completeness in the trial functions has been used. The integration constraint states that the numerical integration of the domain and boundary integrals for Galerkin approximation of a PDE with differential operator L has to be consistent with the test functions $\hat{\Psi}_I$ in the form of (34) for an nth order complete numerical method to achieve the nth order exactness in the Galerkin approximation (passing the nth order patch test).

(2) For $n = 1$, (34) is the integration constraint for the linear patch test as given in [16], which reduces to a divergence condition for a second-order differential operator L such as the elasticity or Poisson problem. Further, stabilized conforming nodal integration introduced in [16] meets the constraint for $n = 1$.

(3) The constraint for constant exactness for self-adjoint PDEs is automatically satisfied when the trial functions possess the partition of unity property.

(4) The integration constraints in (34) act on the test functions $\hat{\Psi}_I$. It is therefore possible, for a given set of nth order complete trial functions and numerical integration methods, to construct test functions, different from the trial functions, to meet the integration constraints. This is demonstrated in Section 4.

3.3. Integration constraint for the Poisson equation

For illustration, consider the two-dimensional Poisson equation, where the operators in (23) and the bilinear form in (24) are defined by

$$L = \nabla^2 \tag{35a}$$
$$B = \boldsymbol{n} \cdot \nabla \tag{35b}$$
$$a(v, u)_\Omega = (\nabla v, \nabla u)_\Omega, \tag{35c}$$

and the trial and test spaces are defined as $U = V = H^1(\Omega)$ and $\Lambda = \Gamma = L^2(\partial\Omega_g)$. Substitution of (35) into (34) gives

$$a\langle \hat{\Psi}_I, \boldsymbol{x}^\alpha \rangle_\Omega = -\langle \hat{\Psi}_I, \nabla^2 \boldsymbol{x}^\alpha \rangle_\Omega + \langle \hat{\Psi}_I, \nabla \boldsymbol{x}^\alpha \cdot \boldsymbol{n} \rangle_{\partial\Omega} \quad \forall I, \ |\alpha| = 0, 1, \ldots, n. \tag{36}$$

By letting $n = 1$, the linear constraints are obtained as

$$\langle \nabla \hat{\Psi}_I \rangle_\Omega = \langle \hat{\Psi}_I \boldsymbol{n} \rangle_{\partial\Omega} \quad \forall I. \tag{37}$$

The integration constraint in (37) is a divergence condition with numerical integration acting on $\hat{\Psi}_I$. Similarly, the quadratic integration constraints are obtained as

$$\langle \hat{\Psi}_{I,1} x \rangle_\Omega = -\langle \hat{\Psi}_I \rangle_\Omega + \langle \hat{\Psi}_I x n_1 \rangle_{\partial\Omega} \quad \forall I \tag{38a}$$
$$\langle \hat{\Psi}_{I,2} y \rangle_\Omega = -\langle \hat{\Psi}_I \rangle_\Omega + \langle \hat{\Psi}_I y n_2 \rangle_{\partial\Omega} \quad \forall I \tag{38b}$$
$$\langle \hat{\Psi}_{I,1} y + \hat{\Psi}_{I,2} x \rangle_\Omega = \langle \hat{\Psi}_I (y n_1 + x n_2) \rangle_{\partial\Omega} \quad \forall I, \tag{38c}$$

and the third order integration constraints are

$$\langle \hat{\Psi}_{I,1} x^2 \rangle_\Omega = -\langle 2\hat{\Psi}_I x \rangle_\Omega + \langle \hat{\Psi}_I x^2 n_1 \rangle_{\partial\Omega} \quad \forall I \tag{39a}$$
$$\langle \hat{\Psi}_{I,2} y^2 \rangle_\Omega = -\langle 2\hat{\Psi}_I y \rangle_\Omega + \langle \hat{\Psi}_I y^2 n_2 \rangle_{\partial\Omega} \quad \forall I \tag{39b}$$
$$\langle 2\hat{\Psi}_{I,1} xy + \hat{\Psi}_{I,2} x^2 \rangle_\Omega = -\langle 2\hat{\Psi}_I y \rangle_\Omega + \langle \hat{\Psi}_I (2xy n_1 + x^2 n_2) \rangle_{\partial\Omega} \quad \forall I \tag{39c}$$
$$\langle \hat{\Psi}_{I,1} y^2 + 2\hat{\Psi}_{I,2} xy \rangle_\Omega = -\langle 2\hat{\Psi}_I x \rangle_\Omega + \langle \hat{\Psi}_I (y^2 n_1 + 2xy n_2) \rangle_{\partial\Omega} \quad \forall I. \tag{39d}$$

Note that for high order exactness, the constraints of each lower order should be satisfied.

3.4. Integration constraint for linear elasticity

The elasticity boundary value problem is stated as:

$$\nabla \cdot \boldsymbol{\sigma} + \boldsymbol{b} = \boldsymbol{0} \quad \text{in } \Omega \tag{40a}$$
$$\boldsymbol{\sigma} \cdot \boldsymbol{n} = \boldsymbol{h} \quad \text{on } \partial\Omega_h \tag{40b}$$
$$\boldsymbol{u} = \boldsymbol{g} \quad \text{on } \partial\Omega_g. \tag{40c}$$

Here, $\boldsymbol{u}$ is the displacement field, $\boldsymbol{\sigma} = \mathbb{C} : \nabla^s \boldsymbol{u}$ is the Cauchy stress tensor, where $\mathbb{C}$ is the elasticity tensor and $\nabla^s \boldsymbol{u} = 1/2(\nabla \otimes \boldsymbol{u} + \boldsymbol{u} \otimes \nabla)$ is the strain tensor. Thus for elasticity we have the following tensorial operators:

$$\boldsymbol{L} = \nabla \cdot \mathbb{C} : \nabla^s \tag{41a}$$

$$\boldsymbol{B} = \boldsymbol{n} \cdot (\mathbb{C} : \nabla^s). \tag{41b}$$

The weak form asks to find $(\boldsymbol{u}, \boldsymbol{\lambda}) \in U \times \Lambda$ such that for all $(\boldsymbol{v}, \boldsymbol{\gamma}) \in V \times \Gamma$, with $U = V = [H^1(\Omega)]^d$ and $\Lambda = \Gamma = [L^2(\partial\Omega_g)]^d$, the following equation holds:

$$a(\boldsymbol{v}, \boldsymbol{u})_\Omega = (\boldsymbol{v}, \boldsymbol{b})_\Omega + (\boldsymbol{v}, \boldsymbol{h})_{\partial\Omega_h} + (\boldsymbol{v}, \boldsymbol{\lambda})_{\partial\Omega_g} + (\boldsymbol{\gamma}, \boldsymbol{u} - \boldsymbol{g})_{\partial\Omega_g}, \tag{42}$$

where the bilinear form and linear forms for elasticity are

$$a(\boldsymbol{v}, \boldsymbol{u})_\Omega = \int_\Omega \nabla^s \boldsymbol{v} : \mathbb{C} : \nabla^s \boldsymbol{u} \, d\Omega \tag{43a}$$

$$(\boldsymbol{v}, \boldsymbol{b})_\Omega = \int_\Omega \boldsymbol{v} \cdot \boldsymbol{b} \, d\Omega \tag{43b}$$

$$(\boldsymbol{v}, \boldsymbol{h})_{\partial\Omega_h} = \int_{\partial\Omega_h} \boldsymbol{v} \cdot \boldsymbol{h} \, d\Gamma \tag{43c}$$

$$(\boldsymbol{v}, \boldsymbol{\lambda})_{\partial\Omega_g} = \int_{\partial\Omega_g} \boldsymbol{v} \cdot \boldsymbol{\lambda} \, d\Gamma. \tag{43d}$$

Consider (40) with the following n^{th} order solution $\boldsymbol{u} = \sum_{|\alpha| \leq n} c_\alpha x^\alpha \equiv \boldsymbol{u}^n$ by using the multi-index notation. Denote the stress tensor corresponding to the displacement field as $\boldsymbol{\sigma}^n = \mathbb{C} : \nabla^s \boldsymbol{u}^n$, and the stress corresponding to x^α as $\boldsymbol{\sigma}^\alpha = \mathbb{C} : \nabla^s x^\alpha$. The boundary conditions and body force associated with this displacement field are

$$\boldsymbol{b} = -\nabla \cdot \boldsymbol{\sigma}^n \quad \text{in } \Omega \tag{44a}$$

$$\boldsymbol{h} = \boldsymbol{\sigma}^n \cdot \boldsymbol{n} \quad \text{on } \partial\Omega_h \tag{44b}$$

$$\boldsymbol{g} = \boldsymbol{u}^n \quad \text{on } \partial\Omega_g. \tag{44c}$$

That is, when the body force and boundary conditions are prescribed as in (44), the solution to (40) is $\boldsymbol{u}^n$. Furthermore, the Lagrange multiplier consistent with the solution $\boldsymbol{u}^n$ is

$$\boldsymbol{\lambda}^n = \boldsymbol{\sigma}^n \cdot \boldsymbol{n} \quad \text{on } \partial\Omega_g, \tag{45}$$

which is the traction on the essential boundary. For the Galerkin form, let us introduce the following approximations:

$$\boldsymbol{u}^h = \sum_{I=1}^{NP} \Psi_I \boldsymbol{u}_I \tag{46a}$$

$$\boldsymbol{v}^h = \sum_{I=1}^{NP} \hat{\Psi}_I \boldsymbol{v}_I \tag{46b}$$

$$\boldsymbol{\lambda}^h = \sum_{I=1}^{NC} \varphi_I \boldsymbol{\lambda}_I \tag{46c}$$

$$\boldsymbol{\gamma}^h = \sum_{I=1}^{NC} \hat{\varphi}_I \boldsymbol{\gamma}_I. \tag{46d}$$

By substituting the approximations (46) into (42) with the exact nodal solution; employing n^{th} order completeness; using prescribed conditions in (44) and the Lagrange multiplier in (45); and

employing numerical integration on (42), the following integration constraints are obtained for elasticity following similar procedures for the scalar equations:

$$\langle \nabla \hat{\Psi}_I \cdot \boldsymbol{\sigma}^\alpha \rangle_\Omega = -\langle \hat{\Psi}_I \nabla \cdot \boldsymbol{\sigma}^\alpha \rangle_\Omega + \langle \hat{\Psi}_I \boldsymbol{\sigma}^\alpha \cdot \boldsymbol{n} \rangle_{\partial\Omega} \quad \forall I, \; |\alpha| = 0, 1, \ldots, n. \tag{47}$$

For illustration purposes, let us consider the two-dimensional ($d = 2$) case. Further manipulation of (47) gives the general two-dimensional integration constraint for elasticity for all I and $|\alpha| = 0, 1, \ldots, n$:

$$\langle \hat{\Psi}_{I,1} \sigma_{11}^\alpha + \hat{\Psi}_{I,2} \sigma_{21}^\alpha \rangle_\Omega = -\langle \hat{\Psi}_I (\sigma_{11,1}^\alpha + \sigma_{21,2}^\alpha) \rangle_\Omega + \langle \hat{\Psi}_I (n_1 \sigma_{11}^\alpha + n_2 \sigma_{21}^\alpha) \rangle_{\partial\Omega} \tag{48a}$$

$$\langle \hat{\Psi}_{I,1} \sigma_{21}^\alpha + \hat{\Psi}_{I,2} \sigma_{22}^\alpha \rangle_\Omega = -\langle \hat{\Psi}_I (\sigma_{21,1}^\alpha + \sigma_{22,2}^\alpha) \rangle_\Omega + \langle \hat{\Psi}_I (n_1 \sigma_{21}^\alpha + n_2 \sigma_{22}^\alpha) \rangle_{\partial\Omega}. \tag{48b}$$

For the linear integration constraint, consider the linear displacement field

$$u_1 = a_{11} x + a_{12} y \tag{49a}$$

$$u_2 = a_{21} x + a_{22} y. \tag{49b}$$

Note that constant terms are omitted because partition of unity in the trial function in general satisfies constant exactness. The stress associated with this displacement is constant:

$$\sigma_{ij} = \mathbb{C}_{ij11} a_{11} + \frac{1}{2} \mathbb{C}_{ij12} (a_{12} + a_{21}) + \frac{1}{2} \mathbb{C}_{ij21} (a_{12} + a_{21}) + \mathbb{C}_{ij22} a_{22}. \tag{50}$$

Substituting (50) into (48) the constraint is reduced to

$$\langle \hat{\Psi}_{I,1} \rangle_\Omega = \langle \hat{\Psi}_I n_1 \rangle_{\partial\Omega} \quad \forall I \tag{51a}$$

$$\langle \hat{\Psi}_{I,2} \rangle_\Omega = \langle \hat{\Psi}_I n_2 \rangle_{\partial\Omega} \quad \forall I, \tag{51b}$$

which is the same as the divergence condition in the Poisson equation (37).

For quadratic exactness, consider the additional quadratic components of the displacement field by

$$u_1 = a_{13} x^2 + a_{14} y^2 + a_{15} xy \tag{52a}$$

$$u_2 = a_{23} x^2 + a_{24} y^2 + a_{25} xy, \tag{52b}$$

which gives the linear stress

$$\sigma_{ij} = \mathbb{C}_{ij11} (2a_{13} x + a_{15} y) + \frac{1}{2} \mathbb{C}_{ij12} (2a_{14} y + a_{15} x + 2a_{23} x + a_{25} y) \\ + \frac{1}{2} \mathbb{C}_{ij21} (2a_{14} y + a_{15} x + 2a_{23} x + a_{25} y) + \mathbb{C}_{ij22} (2a_{24} y + a_{25} x). \tag{53}$$

Substitution of (53) into the constraint (48) results in the following conditions:

$$\langle \hat{\Psi}_{I,1} x \rangle_\Omega = -\langle \hat{\Psi}_I \rangle_\Omega + \langle \hat{\Psi}_I x n_1 \rangle_{\partial\Omega} \quad \forall I \tag{54a}$$

$$\langle \hat{\Psi}_{I,2} y \rangle_\Omega = -\langle \hat{\Psi}_I \rangle_\Omega + \langle \hat{\Psi}_I y n_2 \rangle_{\partial\Omega} \quad \forall I \tag{54b}$$

$$\langle \hat{\Psi}_{I,2} x \rangle_\Omega = \langle \hat{\Psi}_I x n_2 \rangle_{\partial\Omega} \quad \forall I \tag{54c}$$

$$\langle \hat{\Psi}_{I,1} y \rangle_\Omega = \langle \hat{\Psi}_I y n_1 \rangle_{\partial\Omega} \quad \forall I, \tag{54d}$$

which are similar to, but slightly more restrictive than the Poisson equation's constraints (38). Note that for passing quadratic patch test, both (51) and (54) are needed.

Higher-order constraints can be obtained similarly as shown in Appendix A.

4. VARIATIONALLY CONSISTENT INTEGRATION METHODS

Several variationally consistent integration methods are presented in this section. Methods discussed in this section include corrections of existing integration methods that are variationally inconsistent, as well as an extension of SCNI to achieve higher-order exactness.

4.1. Basic ideas

The integration constraints in Section 3 provide a basis for developing a variationally consistent integration method. Completeness of the trial space can be met by using standard shape functions such as the reproducing kernel function given in (1). Straightforward examination of (34) shows that it is possible to select a set of test functions to meet the integration constraints. Here, a procedure is introduced to this end, and it can be applied to arbitrary types of integration.

Let the approximations of scalar trial and test functions be expressed as

$$u^h = \sum_{I=1}^{NP} \Psi_I u_I \tag{55a}$$

$$v^h = \sum_{I=1}^{NP} \hat{\Psi}_I v_I, \tag{55b}$$

where Ψ_I is the trial function which possesses n^{th} order completeness, and consider the test function approximations as

$$\hat{\Psi}_I = \Psi_I + \sum_{|\beta| \leq n} \xi_{\beta I} \hat{\Psi}_I^\beta. \tag{56}$$

Here, it is required that $\{\Psi_I, \hat{\Psi}_I^\beta\}_{|\beta|=1}^n$ be linearly independent. Inserting the trial function and the test functions into the integration constraint for the scalar BVP in (23) yields

$$\sum_{|\beta|=1}^n \xi_{\beta I} \left(a \langle \hat{\Psi}_I^\beta, \boldsymbol{x}^\alpha \rangle_\Omega + \langle \hat{\Psi}_I^\beta, L\boldsymbol{x}^\alpha \rangle_\Omega - \langle \hat{\Psi}_I^\beta, B\boldsymbol{x}^\alpha \rangle_{\partial\Omega} \right) =$$
$$- (a \langle \Psi_I, \boldsymbol{x}^\alpha \rangle_\Omega + \langle \Psi_I, L\boldsymbol{x}^\alpha \rangle_\Omega - \langle \Psi_I, B\boldsymbol{x}^\alpha \rangle_{\partial\Omega}) \qquad \forall I, |\alpha| = 0, 1, \dots, n \tag{57}$$

which can be expressed as

$$\sum_{|\beta|=1}^n A_{\alpha\beta I} \xi_{\beta I} = r_{\alpha I} \quad \forall I, |\alpha| = 0, 1, \dots, n \tag{58}$$

where

$$A_{\alpha\beta I} = a \left\langle \hat{\Psi}_I^\beta, \boldsymbol{x}^\alpha \right\rangle_\Omega + \left\langle \hat{\Psi}_I^\beta, L\boldsymbol{x}^\alpha \right\rangle_\Omega - \left\langle \hat{\Psi}_I^\beta, B\boldsymbol{x}^\alpha \right\rangle_{\partial\Omega} \tag{59a}$$

$$r_{\alpha I} = - (a \langle \Psi_I, \boldsymbol{x}^\alpha \rangle_\Omega + \langle \Psi_I, L\boldsymbol{x}^\alpha \rangle_\Omega - \langle \Psi_I, B\boldsymbol{x}^\alpha \rangle_{\partial\Omega}). \tag{59b}$$

The unknown coefficients $\xi_{\beta I}$ are straightforwardly obtained from (58).

The method resulting from the chosen integration method with trial function and test function formed using (56)–(59) is variationally consistent.

Remarks 4.1

(1) The method is driven from the residual of the numerical integration. If the numerical integration is variationally consistent, that is, $\boldsymbol{\xi}_I = \boldsymbol{0}$, the method is the same as the unmodified method.
(2) The type of numerical integration in the method is arbitrary.
(3) The method allows arbitrarily high order exactness in the Galerkin approximation.
(4) The set of $\{\Psi_I, \hat{\Psi}_I^\beta\}_{|\beta|=1}^n$ is not arbitrary for general problems where solutions may not be in the trial space, and conditions on these functions should be chosen on the basis of stability considerations to be discussed in Section 5.

4.2. Assumed strain variationally consistent integration

The basic approach for constructing the VCI method given in the last section requires solving a local linear system. In this section we seek to decouple the correction equations (58) for enhanced computational efficiency. An assumed strain method is proposed, and this involves a construction of the gradient field to achieve the integration constraints. First, let the test and trial functions be approximated by shape functions with n^{th} order completeness:

$$u^h = \sum_{I=1}^{NP} \Psi_I u_I \tag{60a}$$

$$v^h = \sum_{I=1}^{NP} \Psi_I v_I. \tag{60b}$$

A direct gradient and an assumed gradient are then introduced to the trial and test functions, respectively:

$$\nabla u^h = \sum_{I=1}^{NP} \nabla \Psi_I u_I \tag{61a}$$

$$\tilde{\nabla} v^h = \sum_{I=1}^{NP} \left(\nabla \Psi_I + \sum_{|\beta| \leqslant n} \xi_{\beta I} \nabla \hat{\Psi}_I^{\beta} \right) v_I. \tag{61b}$$

Under this framework, the Galerkin formulation of the Poisson equation seeks $(u^h, \lambda^h) \in U^h \times \Lambda^h$ such that for all $(v^h, \gamma^h) \in V^h \times \Gamma^h$ the following equation holds:

$$\int_{\Omega} \tilde{\nabla} v^h \cdot \nabla u^h \, d\Omega = \int_{\Omega} v^h s \, d\Omega + \int_{\partial \Omega_h} v^h h \, d\Gamma + \int_{\partial \Omega_g} v^h \lambda^h \, d\Gamma + \int_{\partial \Omega_g} \gamma^h (u^h - g) \, d\Gamma, \tag{62}$$

where $\tilde{\nabla}$ is the assumed gradient operator defined by (61b).

Remarks 4.2

Likewise, the Galerkin formulation for elasticity seeks $(\boldsymbol{u}^h, \boldsymbol{\lambda}^h) \in U^h \times \Lambda^h$ such that for all $(\boldsymbol{v}^h, \boldsymbol{\gamma}^h) \in V^h \times \Gamma^h$ the following equation holds:

$$\int_{\Omega} \tilde{\nabla}^s \boldsymbol{v}^h : \mathbb{C} : \nabla^s \boldsymbol{u}^h \, d\Omega = \int_{\Omega} \boldsymbol{v}^h \cdot \boldsymbol{b} \, d\Omega + \int_{\partial \Omega_h} \boldsymbol{v}^h \cdot \boldsymbol{h} \, d\Gamma + \int_{\partial \Omega_g} \boldsymbol{v}^h \cdot \boldsymbol{\lambda}^h \, d\Gamma$$
$$+ \int_{\partial \Omega_g} \boldsymbol{\gamma}^h \cdot (\boldsymbol{u}^h - \boldsymbol{g}) \, d\Gamma, \tag{63}$$

where $\tilde{\nabla}^s \boldsymbol{u}^h = 1/2 \left(\tilde{\nabla} \otimes \boldsymbol{u}^h + \boldsymbol{u}^h \otimes \tilde{\nabla} \right)$.

By using the assumed strain method for the Petrov–Galerkin formulation, it is possible to uncouple the equations in (58). Consider an assumed strain correction for (37) and (51), in two dimensions:

$$\tilde{\nabla} v^h = \sum_{I=1}^{NP} \left(\nabla \Psi_I + R_I \left\{ \begin{matrix} \xi_{1I} \\ \xi_{2I} \end{matrix} \right\} \right) v_I. \tag{64}$$

Here, R_I is taken in its simplest form as

$$R_I(\boldsymbol{x}) = \begin{cases} 1 & \text{if } \boldsymbol{x} \in \text{supp}(\Psi_I(\boldsymbol{x})) \\ 0 & \text{if } \boldsymbol{x} \notin \text{supp}(\Psi_I(\boldsymbol{x})) \end{cases}. \tag{65}$$

Note that different forms for R_I with higher-order continuity can also be considered.

The coefficients are then solved for directly by

$$\xi_{1I} = -(\langle \Psi_{I,1}\rangle_\Omega - \langle \Psi_I n_1\rangle_{\partial\Omega})/\langle R_I\rangle \tag{66a}$$

$$\xi_{2I} = -(\langle \Psi_{I,2}\rangle_\Omega - \langle \Psi_I n_2\rangle_{\partial\Omega})/\langle R_I\rangle. \tag{66b}$$

To satisfy the linear constraints (37) and (51), and quadratic constraints (38) and (54), consider the correction

$$\tilde{\nabla} v^h = \sum_{I=1}^{NP} \left(\nabla\Psi_I + R_I \left\{ \begin{matrix} \xi_{1I} \\ \xi_{2I} \end{matrix} \right\} + S_I \left\{ \begin{matrix} \xi_{3I} \\ \xi_{4I} \end{matrix} \right\} + T_I \left\{ \begin{matrix} \xi_{5I} \\ \xi_{6I} \end{matrix} \right\} \right) v_I, \tag{67}$$

where

$$S_I = R_I \cdot (x - x_I) \tag{68a}$$

$$T_I = R_I \cdot (y - y_I). \tag{68b}$$

The use of (67) uncouples the constraints into two systems of equations

$$A_I \xi_I^1 = r_I^1 \tag{69a}$$

$$A_I \xi_I^2 = r_I^2, \tag{69b}$$

where

$$A_I = \langle P(x - x_I)P^T(x - x_I)R_I\rangle_\Omega \tag{70a}$$

$$P(x) = \{1 \ x \ y\}^T \tag{70b}$$

$$\xi_I^1 = \{\xi_{1I} \ \xi_{3I} \ \xi_{5I}\}^T \tag{70c}$$

$$\xi_I^2 = \{\xi_{2I} \ \xi_{4I} \ \xi_{6I}\}^T \tag{70d}$$

$$r_I^1 = \{r_{1I} \ r_{3I} \ r_{5I}\}^T \tag{70e}$$

$$r_I^2 = \{r_{2I} \ r_{4I} \ r_{6I}\}^T, \tag{70f}$$

and

$$r_{1I} = \langle \Psi_I n_1\rangle_{\partial\Omega} - \langle \Psi_{I,1}\rangle_\Omega \tag{71a}$$

$$r_{2I} = \langle \Psi_I n_2\rangle_{\partial\Omega} - \langle \Psi_{I,2}\rangle_\Omega \tag{71b}$$

$$r_{3I} = \langle \Psi_I n_1(x - x_I)\rangle_{\partial\Omega} - \langle \Psi_I\rangle_\Omega - \langle \Psi_{I,1}(x - x_I)\rangle_\Omega \tag{71c}$$

$$r_{4I} = \langle \Psi_I n_2(x - x_I)\rangle_{\partial\Omega} - \langle \Psi_{I,2}(x - x_I)\rangle_\Omega \tag{71d}$$

$$r_{5I} = \langle \Psi_I n_1(y - y_I)\rangle_{\partial\Omega} - \langle \Psi_{I,1}(y - y_I)\rangle_\Omega \tag{71e}$$

$$r_{6I} = \langle \Psi_I n_2(y - y_I)\rangle_{\partial\Omega} - \langle \Psi_I\rangle_\Omega - \langle \Psi_{I,2}(y - y_I)\rangle_\Omega. \tag{71f}$$

Remarks 4.3

(1) Shifted polynomials $x - x_I$ and $y - y_I$ have been used in the construction of the assumed strain field to yield a symmetric matrix A_I. This assumed strain field in (61) along with the form of residual ensures the invertibility of A_I, so long as sufficient nodes are under the cover of the kernel function (65) for linear independency.

(2) The form of the assumed strain fields in (61), (64), and (67) allows decoupling of the integration constraint correction equations. Further, the form chosen appears stable according to Section 5.2. Numerical observation demonstrates remarkable stability of the assumed strain method over a direct gradient approach.

(3) The additional computational cost of using (61) is roughly the cost of integration of a body force and a total boundary term. It has been observed in large scale computations that the expense for linear VCI correction is negligible and therefore it is much more effective than using higher-order quadrature rules.

5. STABILITY ANALYSIS

Whenever a Petrov–Galerkin method such as the assumed strain VCI method presented in Section 4.2 is used, stability may become an issue. In this section, abstract stability estimates are presented for both Bubnov–Galerkin and Petrov–Galerkin methods. It is noted that for the assumed strain VCI method, the stability analysis of the Petrov–Galerkin method can be simplified and stability can be shown in terms of coercivity rather than an inf-sup condition.

5.1. Stability estimates for Bubnov–Galerkin and Petrov–Galerkin methods

Here, for clarity and simplicity, it is assumed that the test and trial functions are kinematically admissible so that the Lagrange multipliers in (29) are not taken into account. Consider the following weak form statement: find $u^h \in V^h$ such that

$$a\left(v^h, u^h\right)_\Omega = F\left(v^h\right) \quad \forall v^h \in V^h. \tag{72}$$

For Bubnov–Galerkin methods, the existence of a unique solution $u^h \in V^h$ to the abstract discrete problem is a direct consequence of the Lax–Milgram theorem, provided that the linear form F is continuous and that the bilinear form a is continuous and coercive. Note that in the Bubnov–Galerkin method, a is defined on $V^h \times V^h$. The stability of the approximate solution u^h can be easily verified by means of the coercivity of the bilinear form a, that is,

$$a\left(u^h, u^h\right)_\Omega \geqslant \rho \|u^h\|_V^2 \quad \forall u^h \in V^h, \tag{73}$$

with appropriate norm $\|\cdot\|_V$ on V, holds for $\rho > 0$, because, by the continuity of F and the variational equation (72), one obtains

$$\|u^h\|_V \leqslant \frac{1}{\rho} \|F\|_{V'} \tag{74}$$

where $\|\cdot\|_{V'}$ denotes the dual norm of $\|\cdot\|_V$.

In the case of Petrov–Galerkin methods, the bilinear form a is defined on $V^h \times U^h$. Existence and uniqueness of the discrete solution $u^h \in U^h$ now mainly relies on an inf-sup condition, which can be equivalently expressed as

$$\sup_{v^h \in V^h} \frac{a\left(v^h, u^h\right)_\Omega}{\|v^h\|_V} \geqslant \kappa \|u^h\|_U \quad \forall u^h \in U^h, \tag{75}$$

with $\kappa > 0$ and appropriate norm $\|\cdot\|_U$ on U. By using the variational equation (72), stability can be shown in the same way as the Bubnov–Galerkin method and yields the estimate

$$\|u^h\|_U \leqslant \frac{1}{\kappa} \|F\|_{V'}. \tag{76}$$

Summarizing, both Bubnov–Galerkin and Petrov–Galerkin methods lead to a similar stability estimate. However, in the case of Bubnov–Galerkin methods, the stability estimate relies on the coercivity condition (73). In this case, the coercivity of a in the discrete setting is inherited from the coercivity of its continuous counterpart and therefore, in general, is easy to show. In the case of Petrov–Galerkin methods, the stability estimate relies on the inf-sup condition (75) and it requires well-balanced spaces U^h and V^h.

5.2. Stability analysis

Next, stability analysis is presented for the assumed strain VCI method. Because of the form of the proposed correction (61), the stability analysis of this Petrov–Galerkin method can be carried out by means of the coercivity of the bilinear form as shown in (73) rather than fulfilling an inf-sup

condition of the form (75). Without loss of generality, considerations are restricted to the case of a Poisson problem.

With the concept of assumed strains in the Petrov–Galerkin framework, and with quadratures considered in the linear products, the bilinear form takes the form

$$\tilde{a}\langle v^h, u^h\rangle_\Omega = \langle \tilde{\nabla} v^h, \nabla u^h\rangle_\Omega. \tag{77}$$

Inserting the ansatz (64) into the above, and setting $v^h = u^h$ (because $V^h = U^h$) we arrive at

$$\tilde{a}\langle u^h, u^h\rangle_\Omega = \sum_{I=1}^{NP} \sum_{J=1}^{NP} u_I \{\langle \nabla\Psi_I, \nabla\Psi_J\rangle_\Omega + \langle R_I\boldsymbol{\xi}_I, \nabla\Psi_J\rangle_\Omega\} u_J. \tag{78}$$

Performing integration by parts on this term, we obtain

$$\tilde{a}\langle u^h, u^h\rangle_\Omega = \sum_{I=1}^{NP} \sum_{J=1}^{NP} u_I \{\langle \nabla\Psi_I, \nabla\Psi_J\rangle_\Omega - \langle \nabla R_I \cdot \boldsymbol{\xi}_I + \nabla\cdot\boldsymbol{\xi}_I R_I, \Psi_J\rangle_\Omega + \langle \boldsymbol{\xi}_I \cdot \boldsymbol{n} R_I, \Psi_J\rangle_{\partial\Omega}\} u_J. \tag{79}$$

Note that the second term vanishes if (65) is employed, and we have

$$\tilde{a}\langle u^h, u^h\rangle_\Omega = \sum_{I=1}^{NP} \sum_{J=1}^{NP} u_I \{\langle \nabla\Psi_I, \nabla\Psi_J\rangle_\Omega - \langle \nabla\cdot\boldsymbol{\xi}_I R_I, \Psi_J\rangle_\Omega + \langle \boldsymbol{\xi}_I \cdot \boldsymbol{n} R_I, \Psi_J\rangle_{\partial\Omega}\} u_J. \tag{80}$$

As can be seen, the stability of our proposed Petrov–Galerkin methods depends solely on the correction coefficients $\boldsymbol{\xi}_I$, and is therefore stable for sufficiently 'small' correction coefficients $\boldsymbol{\xi}_I$ and their gradients. This also becomes clear, because in this case the quadrature versions of the integrals approach the exact integrals. In other words, the coefficients are dependent on the magnitude of the residual of the associated integration constraint to be satisfied. Therefore, increasing the accuracy of domain integration should yield an increasingly stable correction method for the technique proposed herein. Furthermore, increasing the support in (65) gives an even more stable result because of the coefficients in (66) being smaller on a whole.

Note that in the special cases of small corrections and pure homogeneous essential boundary conditions or for $\xi_1 = \xi_2 = 0$ on the boundary $\partial\Omega$ we obtain

$$\tilde{a}\langle u^h, u^h\rangle_\Omega = \sum_{I=1}^{NP} \sum_{J=1}^{NP} u_I \{\langle \nabla\Psi_I, \nabla\Psi_J\rangle_\Omega\} u_J. \tag{81}$$

The stability of such a discrete bilinear form can be analyzed by the coercivity condition with standard procedures.

6. NUMERICAL EXAMPLES

Because the boundary condition enforcement should attest to the strong form as described in Section 3, Nitsche's method is used with a penalty parameter of $10^3/h$ for the Poisson equation and $10^3 E/h$ for elasticity, where E is Young's modulus. Unless otherwise stated, quartic B-spline kernels are used in all examples with normalized supports for linear, quadratic, and cubic bases equal to 2.0, 3.0, and 4.0, respectively. The form of VCI used in all examples is the method described in Section 4.2.

6.1. Patch tests in one dimension

Consider the following one-dimensional model problem on the domain $\Omega = (0, 1)$:

$$u_{,xx}(x) + s(x) = 0 \quad \text{in } \Omega, \tag{82}$$

with boundary conditions

$$u(0) = 0, \ u(1) = g. \tag{83}$$

The following cases for the source term $s(x)$ are examined that correspond to the linear, quadratic, and cubic patch tests for case 1, 2, and 3, respectively, and a high order solution is considered for case 4:

$$\text{Case 1: } s(x) = 0, \qquad\qquad g = 1 \qquad\qquad (84a)$$

$$\text{Case 2: } s(x) = 8, \qquad\qquad g = 1 \qquad\qquad (84b)$$

$$\text{Case 3: } s(x) = 8 + 16x, \qquad g = 1 \qquad\qquad (84c)$$

$$\text{Case 4: } s(x) = 4\pi^2 \sin(2\pi x), \quad g = 0. \qquad\qquad (84d)$$

For these cases, consider the nonuniform node distribution of 26 nodes shown in Figure 8.

Here, single point GI, DNI, and their VCI counterparts are employed, herein denoted VC-GI and VC-DNI, respectively. The orders of completeness in the approximation are chosen to be 1, 2, and 3 for linear, quadratic, and cubic patch tests, respectively, for all the integration methods tested. The kernel supports in this example are normalized by the larger distance between the nodal neighbors.

Figure 8. Irregular node distribution in one dimension.
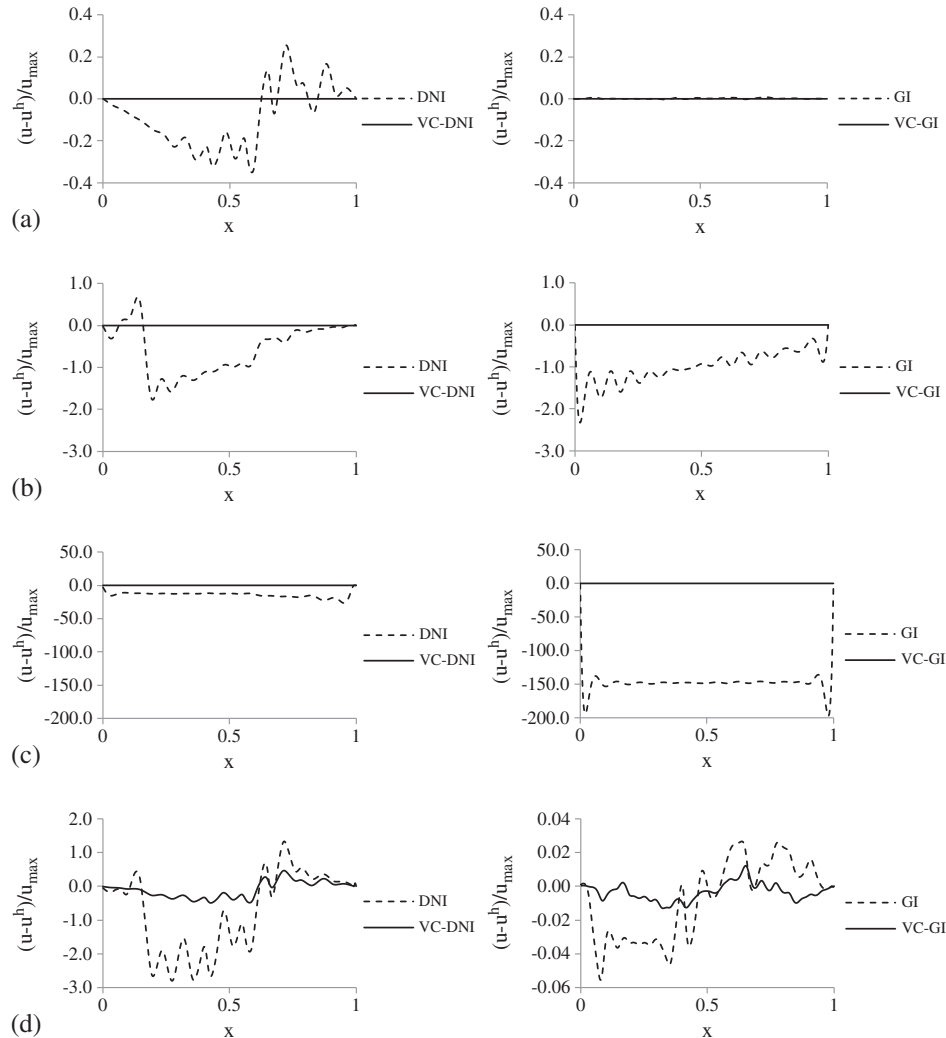
Figure 9. Errors in one-dimensional patch tests: (a) case 1, linear variationally consistent integration (VCI); (b) case 2, quadratic VCI; (c) case 3, cubic VCI; and (d) case 4, linear VCI.

For the assumed strain method, (60) and (61) is used with the following functions chosen for the assumed gradient for increasing orders of n for VCI:

$$\hat{\Psi}^n_{I,x}(x) = R_I(x)(x - x_I)^{n-1}. \tag{85}$$

First, case 1 is examined with linear VCI. Next, for cases 2 and 3, quadratic VCI, and cubic VCI are employed, respectively. Lastly, case 4 is examined with linear basis and linear VCI. The errors for the four analyses are shown in Figure 9. Variationally consistent integration is seen to pass arbitrarily high order patch tests as well as decrease the error for high order problems.

6.2. Patch tests for the 2D Poisson equation

Consider the Poisson problem (8) with the domain taken as $\Omega : (-1, 1) \times (-1, 1)$ with the boundary decomposition $\partial\Omega_h : 0 \leqslant x \leqslant 1$, $y = 1$, and $\partial\Omega_g = \partial\Omega \setminus \partial\Omega_h$.

Let the prescribed body force and boundary conditions for (8) be consistent with a linear solution

$$u = x + 2y. \tag{86}$$

The domain discretization and integration schemes are depicted in Figure 10. SNNI smoothing zones are chosen to extend over the boundary so that completeness is maintained (see Remarks 2.1) for the quadratic patch tests. Nodes are also moved into the numerical centroid (21) of the Voronoi cells so that the gradient consistency of the smoothed strain is maintained for SCNI (see Remarks 2.1).

Linear bases are introduced with the standard methods along with linear VCI employed as correction of variationally inconsistent integration methods. The error for GI, DNI, and SNNI is shown in Table III, along with their VCI counterparts (denoted herein VC-SNNI for SNNI with VCI) and SCNI. It is seen that the proposed VCI enables arbitrary types of integration to pass the linear patch test.

Now consider the Poisson equation (8), again on $(-1, 1) \times (-1, 1)$, with the same boundary decomposition but with source term and boundary conditions consistent with the quadratic solution

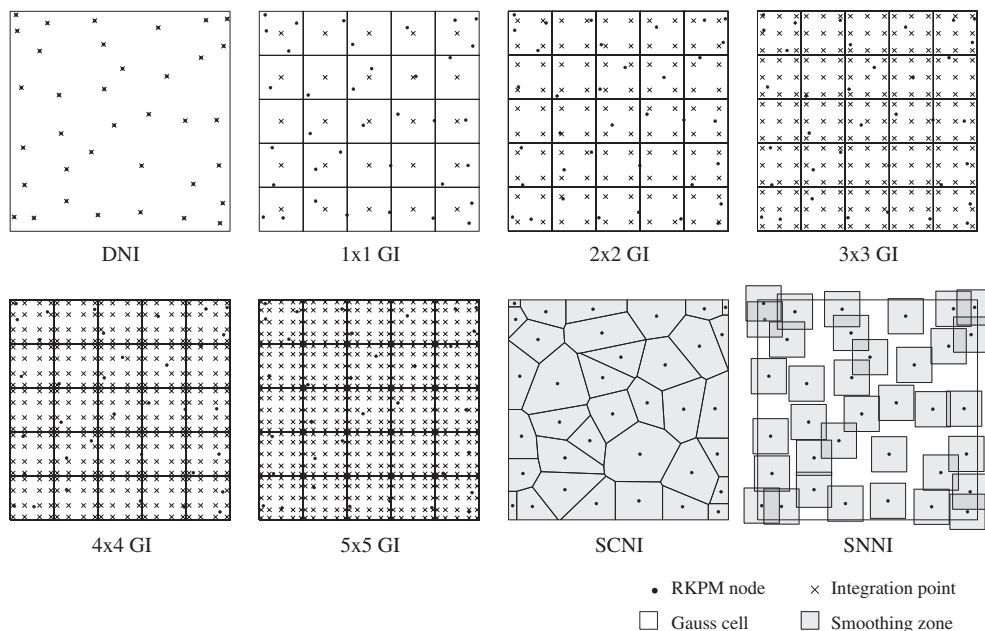$$u = 0.1x + 0.3y + 0.8x^2 + 1.2xy + 0.6y^2. \tag{87}$$

Figure 10. Domain discretization and integration schemes for patch tests.

Table III. L^2 norm of error for various integration methods in linear patch test of Poisson equation.

Method	Standard	VCI
SCNI	1.20E-13	—
SNNI	0.0903225	5.28E-14
DNI	0.1200994	1.24E-13
1×1 GI	0.1249480	1.03E-13
2×2 GI	0.0233911	4.11E-14
3×3 GI	0.0060938	4.42E-14
4×4 GI	0.0020703	6.39E-14
5×5 GI	0.0007464	3.81E-14

SCNI, stabilized conforming nodal integration; SNNI, stabilized nonconforming nodal integration; DNI, direct nodal integration; GI, Gauss integration.

Table IV. L^2 norm of error for various integration methods in quadratic patch test of Poisson equation.

Method	Standard	VCI
SCNI	0.1319736	1.69E-13
SNNI	0.1702456	1.88E-13
DNI	0.2183826	8.80E-14
1×1 GI	0.2298442	3.60E-13
2×2 GI	0.0088438	1.69E-13
3×3 GI	0.0017520	1.31E-13
4×4 GI	0.0003855	1.80E-13
5×5 GI	0.0000731	1.25E-13

VCI, variationally consistent integration; SCNI, stabilized conforming nodal integration; SNNI, stabilized nonconforming nodal integration; DNI, direct nodal integration; GI, Gauss integration.

As required to pass the quadratic patch test, a quadratic basis is used to construct the RKPM shape functions. The discretization and integration schemes depicted in Figure 10 are again employed with standard methods and their quadratic VCI counterparts, and the error is shown in Table IV. Note that SCNI passes only the linear patch test, and it requires VCI to pass the quadratic patch test (SCNI with quadratic VCI denoted herein as VC-SCNI).

6.3. Patch tests for elasticity

For the linear patch test, let the prescribed body force and boundary conditions for (40) be consistent with a linear solution as follows:

$$\boldsymbol{u} = \left\{ \begin{array}{c} 0.1x + 0.3y \\ 0.2x + 0.4y \end{array} \right\}. \tag{88}$$

For this problem and all elasticity patch tests, the plane strain formulation is used with Young's modulus E equal to 100 kN/m^2 and Poisson's ratio ν equal to 0.3, and a domain $\Omega = (-1\text{m}, 1\text{m}) \times (-1\text{m}, 1\text{m})$ is discretized by 25 RKPM nodes. The decomposition of boundary condition is the same as that of Section 6.2. The four integration methods considered previously are employed and are depicted in Figure 10.

Linear bases are introduced along with linear VCI; the error is presented in Table V. It can be seen that the standard methods violate the integration constraint, and VCI precludes the situation for every integration scheme. The qualitative behavior of the solutions is shown in Figure 11, and spurious deformations are seen to take place for methods without VCI.

Linear exactness also means exactness in the constant stresses. For illustration, the shear stresses are plotted in Figure 12 for the standard methods and for VCI. It is seen that the variationally consistent methods can exactly represent this constant stress state in the domain. Note the performance of SNNI over DNI and 1×1 GI, which gives far less spurious stress in the domain.

Table V. L^2 norm of error for various integration methods in linear patch test of elasticity problem.

Method	Standard	VCI
SCNI	8.66E-14	—
SNNI	0.0531788	3.21E-14
DNI	0.0648288	3.42E-14
1×1 GI	0.0810321	2.63E-14
2×2 GI	0.0118552	2.32E-14
3×3 GI	0.0023590	3.38E-14
4×4 GI	0.0008091	2.56E-14
5×5 GI	0.0003097	2.71E-14

VCI, variationally consistent integration; SCNI, stabilized conforming nodal integration; SNNI, stabilized nonconforming nodal integration; DNI, direct nodal integration; GI, Gauss integration.
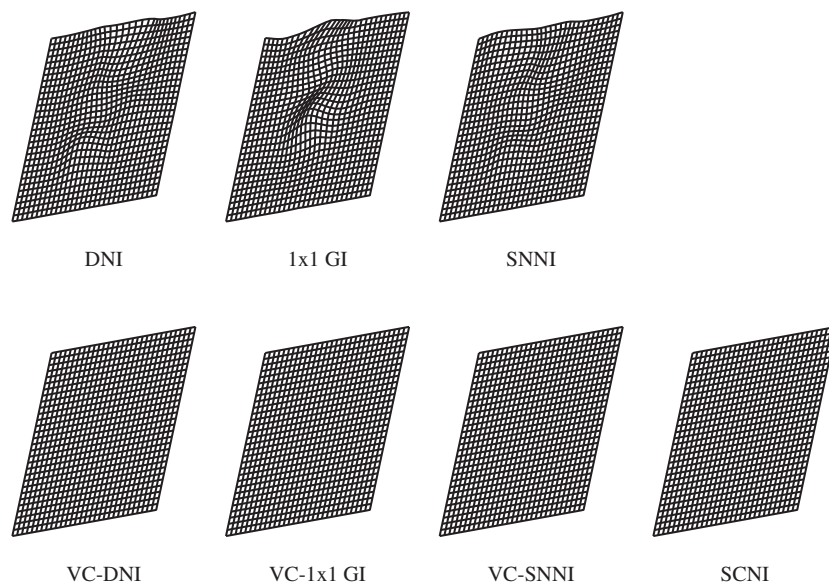
Figure 11. Solutions for elastic linear patch test.
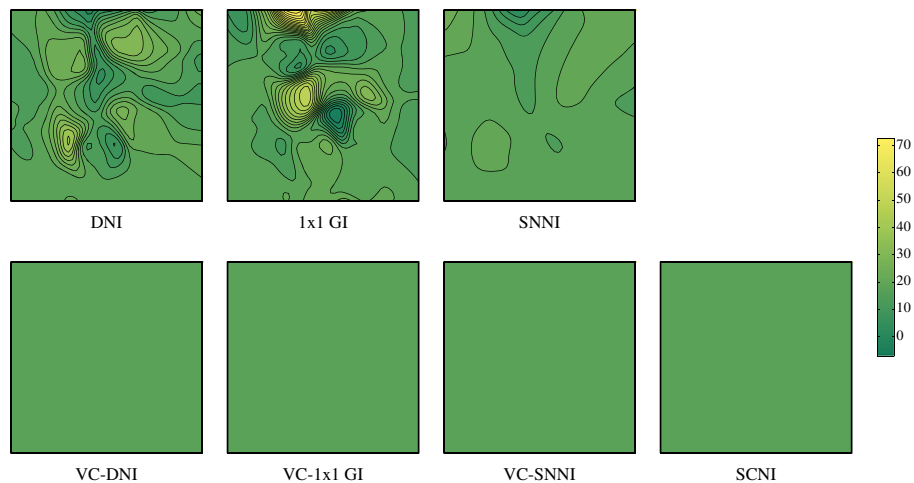
Figure 12. Stress distributions in elasticity linear patch test, units in kN/m^2.

Table VI. L^2 norm of error for various integration methods in quadratic patch test of elasticity problem.

Method	Standard	VCI
SCNI	0.0622307	1.09E-13
SNNI	0.1081434	1.02E-13
DNI	0.1168936	1.46E-13
1×1 GI	0.1660389	1.44E-13
2×2 GI	0.0064088	5.73E-14
3×3 GI	0.0011188	9.68E-14
4×4 GI	0.0002739	5.68E-14
5×5 GI	0.0000572	4.28E-14

VCI, variationally consistent integration; SCNI, stabilized conforming nodal integration; SNNI, stabilized nonconforming nodal integration; DNI, direct nodal integration; GI, Gauss integration.

For the quadratic patch test, consider the prescribed conditions (44) for the elasticity BVP (40) with solution

$$u = \left\{ \begin{array}{l} 0.12x + 0.14y + 0.16x^2 + 0.18xy + 0.20y^2 \\ 0.11x + 0.13y + 0.15x^2 + 0.10xy + 0.21y^2 \end{array} \right\}. \tag{89}$$

Here quadratic bases are introduced; the errors for the various methods are given in Table VI, and again it is seen that the variationally consistent methods are able to pass the patch test. In the case of methods that do not pass the patch test, oscillations are even more severe than in the linear patch test as seen in Figure 13, and the corresponding spurious stresses are shown in Figure 14. It can be observed that stresses obtained by the standard methods can have error on the same order of the exact stress itself. Gauss integration performs particularly poor, whereas DNI provides better results here. Note SCNI and SNNI generate far less error in the stress compared with the other variationally inconsistent methods.

6.4. Convergence in the Poisson equation

Consider the Poisson equation (8) with the source term and homogeneous boundary conditions given as in (10). Here GI, DNI, and SNNI are employed with their VCI counterparts along with SCNI, and VC-SCNI if applicable. The domain discretization and subsequent uniform refinements are depicted in Figure 3. Normalized supports for all convergence studies are taken as 1.75 and 2.75 for linear and quadratic basis, respectively.
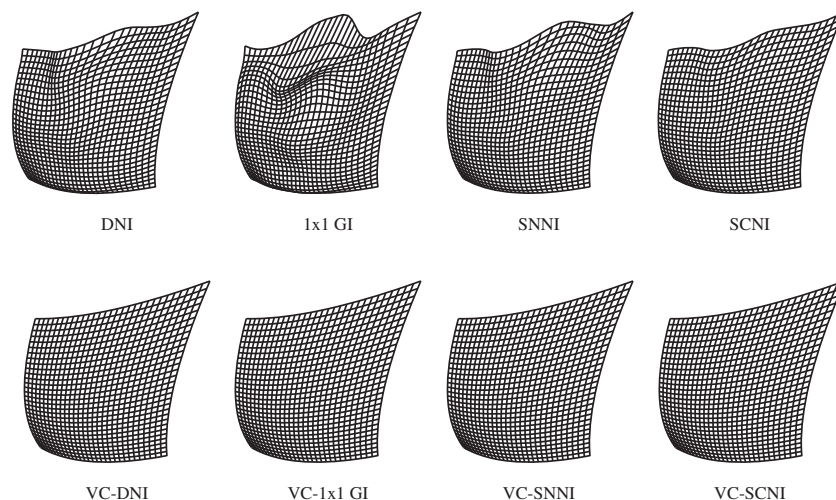

Figure 13. Solutions for quadratic elastic patch test in quadratic patch test of elasticity problem.
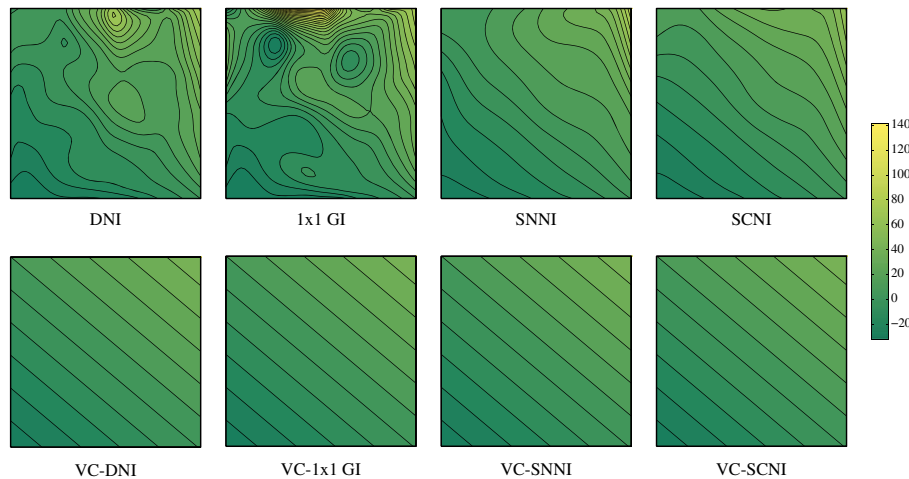
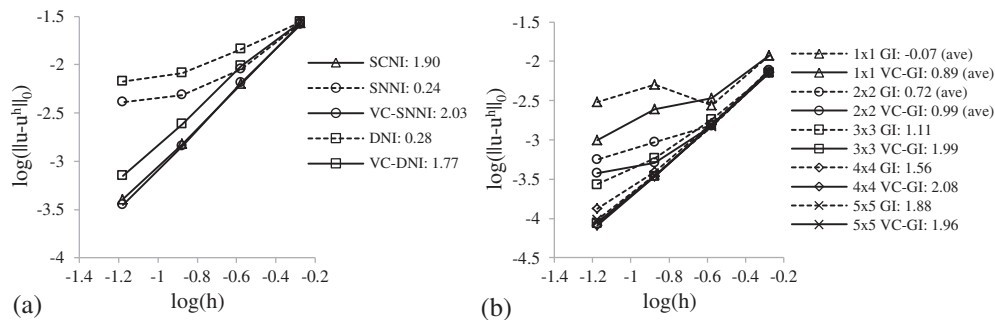Figure 14. Shear stress distributions for quadratic elastic patch test of elasticity problem, units in kN/m^2.

Figure 15. Convergence of error in the L^2 norm for standard methods with first-order completeness and linear variationally consistent integration (VCI) methods for Poisson problem by using (a) nodal methods and (b) Gauss integration (GI).

The L^2 norm of the error for nodal methods with first-order bases in the trial functions is plotted against the length h in Figure 15(a), and it is seen that VCI improves the rate of convergence and accuracy for all methods shown. Note the strikingly similar behavior of VC-DNI, VC-SNNI, and SCNI with respect to error and convergence in the L^2 norm. The rates are nearly restored and fully restored for VC-DNI and VC-SNNI, respectively. Figure 15(b) shows the convergence plots for increasing orders of GI with their VCI counterparts. It is seen that convergence and error are superior for all cases by using the variationally consistent counterparts. Increasing orders GI achieves optimal rate with 3×3 VC-GI, whereas 5×5 GI is necessary for optimal convergence.

Variationally consistent integration also performs well regarding solution derivatives; the convergence of the nodal methods with first-order bases in the trial functions in the H^1 semi-norm is shown in Figure 16(a). In the case of DNI and SNNI, the error is seen to have poor rates, whereas VC-DNI and VC-SNNI maintain near optimal and optimal convergence, respectively.

Figure 16(b) shows the convergence in the H^1 semi-norm for increasing orders of GI. It is seen that VCI is able to reduce the severity of the error in the diverging result of 1×1 GI, and that 2×2 VC-GI can achieve optimum convergence, whereas 5×5 GI can only partially restore optimum convergence.

A study is performed with quadratic VCI with the refinements shown in Figure 3. Figure 17(a) shows the convergence of the error in the L^2 norm for nodal methods with second-order bases in the trial functions with their quadratic VCI counterparts. Here one can see again the similarity of VCI nodal methods with respect to error and convergence. VC-SCNI, VC-SNNI, and VC-DNI have enhanced convergence although the rate is not fully recovered.
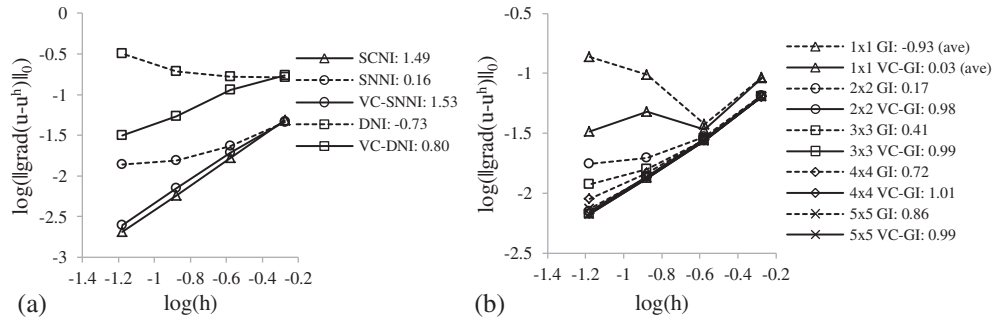
Figure 16. Convergence of error in the H^1 semi-norm for standard methods with first-order completeness and linear variationally consistent integration (VCI) methods for Poisson problem by using (a) nodal methods and (b) Gauss integration (GI).
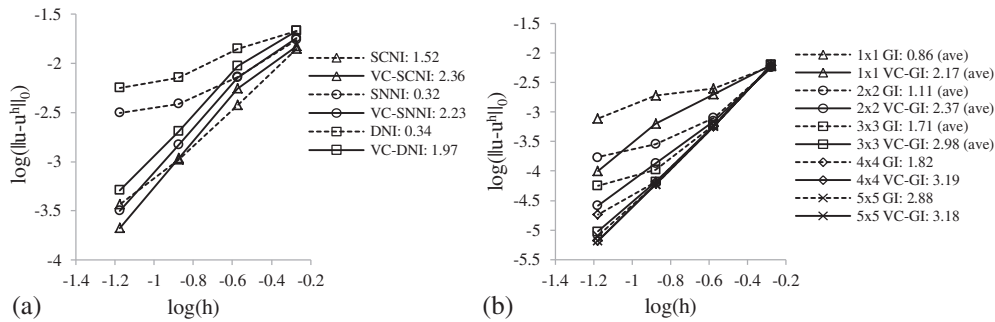

Figure 17. Convergence of error in the L^2 norm for standard methods with second-order completeness and quadratic variationally consistent integration (VCI) methods for Poisson problem by using (a) nodal methods and (b) Gauss integration (GI).

Figure 17(b) shows the convergence of the error in the L^2 norm for increasing orders of Gauss integration, and again the error and convergence is superior in all cases of variationally consistent integration. The rate is fully restored to the theoretical rate with 3×3 VC-GI, and further improved with higher-order integration. In contrast, 5×5 GI is necessary to nearly restore cubic convergence.

Figure 18(a) shows the convergence plots for the H^1 semi-norm for quadratic standard and quadratic VCI nodal methods, where the VCI nodal methods again are superior to their counterparts. Convergence is nearly restored in the case of the smoothed nodal methods with VCI corrections, and partially restored for VC-DNI. The convergence in the H^1 semi-norm for increasing orders of GI is
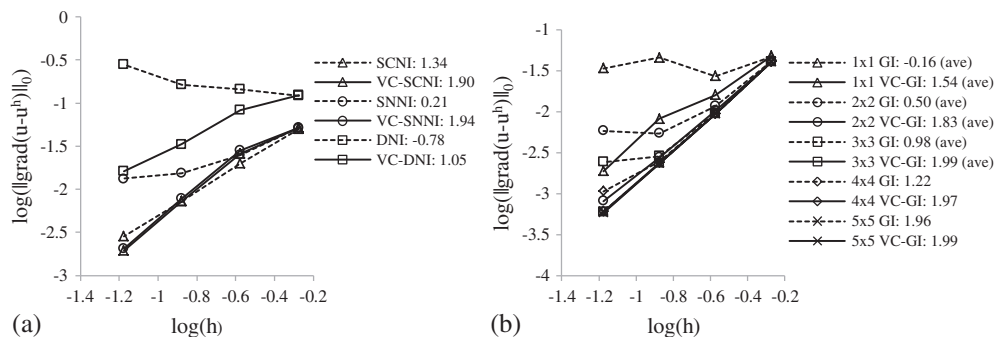

Figure 18. Convergence of error in the H^1 semi-norm for standard methods with second order completeness and quadratic variationally consistent integration (VCI) methods for Poisson problem by using (a) nodal methods and (b) Gauss integration (GI).
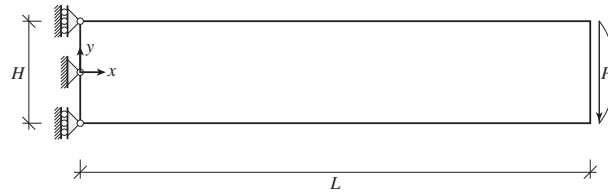
Figure 19. Cantilever beam with shear load.

shown in Figure 18(b). Here it is seen that the optimal rate is obtained with 3×3 VC-GI, whereas for standard GI, 5×5 GI is necessary to restore optimal rates.

6.5. Cantilever beam

A cantilever beam is considered with a parabolic shear load at one end, and the problem statement is shown in Figure 19. The plane stress assumption is made, and the exact solution to the problem is

$$u_x = \frac{Py}{6EI}\left[(6L - 3x)x + (2 + \nu)\left(y^2 - \frac{H^2}{4}\right)\right] \tag{90a}$$

$$u_y = -\frac{P}{6EI}\left[(L - x)3\nu y^2 + (4 + 5\nu)\frac{H^2}{4}x + (3L - x)x^2\right], \tag{90b}$$

where $I = H^3/12$ is the moment of inertia of the beam and P is the resultant of the shear stress applied. The load P was chosen to be 10^3 kN, and was applied according to the traction resulting from (90).

The domain is taken to be $\Omega = (0\text{m}, 10\text{m}) \times (-1\text{m}, 1\text{m})$ with material constants $E = 30 \cdot 10^6$ kN/m^2 and $\nu = 0.3$. The domain is discretized with two steps of refinement with nonuniform node distributions, shown in Figure 20. Linear basis is introduced with 1x1 GI, DNI, and SNNI, and the linear assumed strain correction is used for each method, denoted as 1×1 VC1-GI, VC1-DNI, and VC1-SNNI, respectively. Quadratic VCI is also employed for each integration method with linear bases, denoted as 1×1 VC2-GI, VC2-DNI, and VC2-SNNI, respectively. SCNI is again employed for comparison. The reason for using linear bases with quadratic correction is to examine how higher-order corrections can improve solution accuracy without increasing the order of bases.

Tip displacement accuracy for various VCI methods is shown in Table VII. Although VC1 clearly enhances accuracy over the standard counterparts, VC2 improves the accuracy even further. Note that tip displacement in 1×1 GI actually diverges with refinement, whereas the two 1×1 VC-GI methods converge. We also see that VC2-SNNI provides the best results aside from SCNI.

The shear stress of the fine model along $x = L/2$ for SCNI, standard integrations and their variationally consistent counterparts are shown in Figures 21–24. Looking over the figures we see that SCNI and VC2-SNNI give the most accurate stress results compared with all other methods,
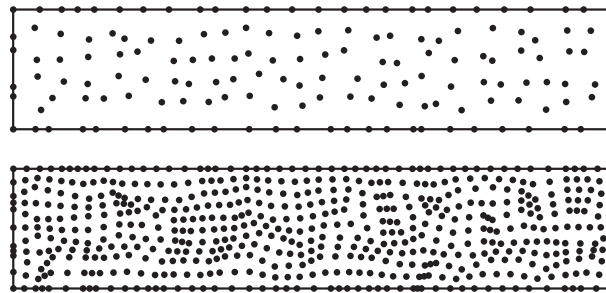

Figure 20. Discretizations for beam problem.

Table VII. Tip displacement accuracy for various integration methods.

Nodes	1×1 GI	1×1 VC1-GI	1×1 VC2-GI	SNNI	VC1-SNNI	VC2-SNNI	DNI	VC1-DNI	VC2-DNI	SCNI
156	142.3	115.0	105.3	132.7	118.6	101.9	171.0	118.1	96.3	99.4
561	147.5	108.0	105.1	106.5	102.0	99.3	107.1	97.4	98.7	100.0

VCI, variationally consistent integration; SCNI, stabilized conforming nodal integration; SNNI, stabilized nonconforming nodal integration; DNI, direct nodal integration; GI, Gauss integration.

although the VC1-SNNI and VC2-DNI results are also satisfactory. It is seen that all VCI methods have significantly improved accuracy compared with their standard counterparts, which are particularly inaccurate in the case of 1×1 GI and DNI. Although VCI-1 can provide improved results for all methods, the stress field is further enhanced using VCI-2, particularly for SNNI and DNI.
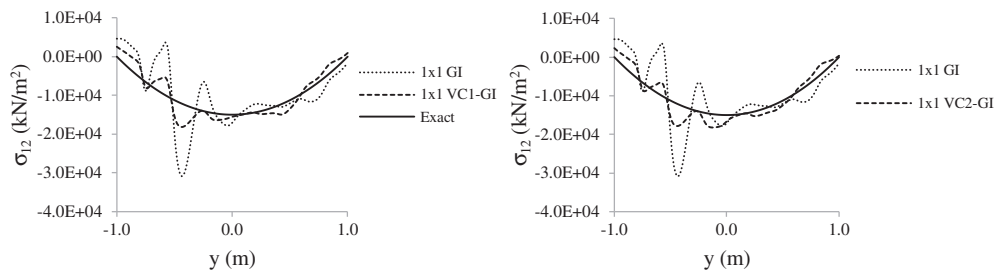

Figure 21. Shear stress along $x = L/2$ for 1×1 Gaussian integration (GI), 1×1 variationally consistent Gaussian integration VC1-GI, and 1×1 VC2-GI.
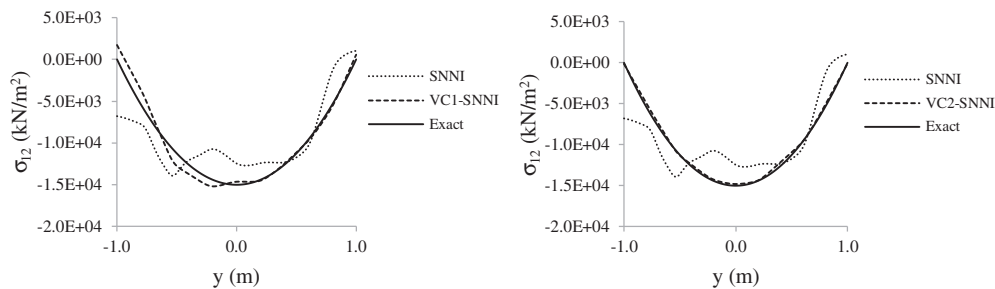

Figure 22. Shear stress along $x = L/2$ for stabilized nonconforming nodal integration (SNNI), variationally consistent stabilized nonconforming nodal integration VC1-SNNI, and VC2-SNNI.
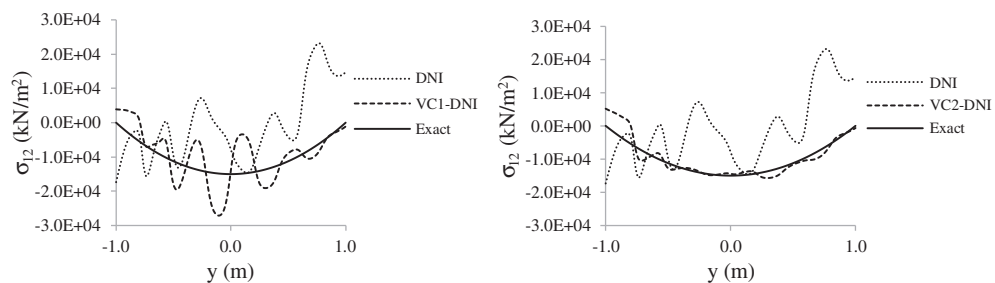

Figure 23. Shear stress along $x = L/2$ for direct nodal integration (DNI), variationally consistent direct nodal integration VC1-DNI, and VC2-DNI.
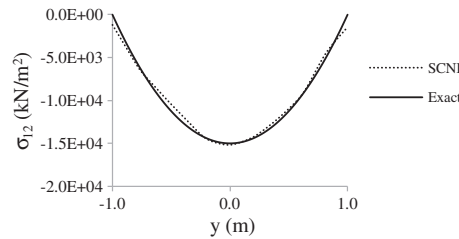
Figure 24. Shear stress along $x = L/2$ for stabilized conforming nodal integration method (SCNI).

7. CONCLUSIONS

The approximation functions commonly employed in the Galerkin meshfree methods, such as MLS and RK, are capable of reproducing monomials of arbitrary order in arbitrary discretizations. This completeness property, however, does not guarantee optimal rate of convergence in the Galerkin solution of PDEs if the domain integration is not sufficiently accurate. Because the MLS/RK approximation functions are of rational type with overlapping supports, achieving high accuracy in the domain integration of Galerkin meshfree methods often requires considerably fine integration cells or very high quadrature order. This paper proposes an alternative approach to achieve optimal convergence consistent with the order of completeness in the approximation by introducing a variationally consistent integration formulation. This method uses integration constraints constructed from the discrete version of the weak equation as the basis for development, and it can be used as the correction for several commonly used domain integration methods to achieve optimal convergence.

This work begins with deriving the condition for n^{th} order exactness in the Galerkin approximation of PDEs. This condition is a generalization of the linear integration constraint [16], and the numerical methods that meet this condition are called VCI methods. The resulting n^{th} order variational consistency condition of a given PDE states that the numerical integration by parts conditions should hold for the inner product between the test functions and the differential operator acting on the nth order monomials. If the domain and boundary integration methods of the Galerkin weak equation are consistent with the test function, the differential operator, and the boundary operator following the integration constraint, then the optimal convergence rates can be achieved.

The nth order integration constraint has been applied to several PDEs to arrive at constraints specific to the problem and the desired order of exactness in the Galerkin approximation. A method has been proposed to correct integration methods that violate the integration constraints, such as DNI, GI, and SNNI. It is shown that improved accuracy and convergence is attained for variationally consistent integration, particularly in the derivatives of the solution. Several important observations are summarized as follows:

(1) Variationally consistent nodal integration methods show promise with performance similar to SCNI, particularly VC-SNNI.
(2) VC-SNNI is in general more accurate than VC-DNI, although similar convergence rates have been achieved between the two methods.
(3) VCI for GI has been shown to supplement the convergence rates for lower order GI so that optimal convergence rates can be restored with far fewer quadrature points than would otherwise be required.
(4) Integration methods that are far from being variationally consistent, such as using one point Gauss quadrature for achieving quadrature exactness, could violate the stability condition and result in suboptimal convergence even with the proposed correction.
(5) SCNI that was developed for linear exactness can be corrected to achieve higher-order exactness by using VC-SCNI.
(6) Corrected SNNI, namely VC-SNNI, possesses similar convergence and accuracy performance as that of SCNI, but offers a considerable simplicity over SCNI without the need of Voronoi cells in the strain smoothing.

(7) Without increasing the order of bases, the second-order correction (VC2) further enhances the solution accuracy over the variationally inconsistent method with first-order correction (VC1).

The extension of this work to nonlinear mechanics, and plate and shell problems is under investigation, and the results will be published in forthcoming papers.

APPENDIX A: CUBIC CONSTRAINT FOR ELASTICITY

Similar to the procedures given in Section 3, arbitrarily high order constraints can be obtained for any PDE. Here the cubic constraint is derived for elasticity.

For cubic exactness in elasticity, consider the additional cubic components of the displacement field

$$u_1 = a_{16}x^3 + a_{17}x^2y + a_{18}xy^2 + a_{19}y^3 \tag{A.1a}$$

$$u_2 = a_{26}x^3 + a_{27}x^2y + a_{28}xy^2 + a_{29}y^3, \tag{A.1b}$$

which gives quadratic stresses

$$
\begin{aligned}
\sigma_{ij} = {} & \mathbb{C}_{ij11}(3a_{16}x^2 + 2a_{17}xy + a_{18}y^2) \\
& + \frac{1}{2}\mathbb{C}_{ij12}(a_{17}x^2 + 2a_{18}xy + 3a_{19}y^2 + 3a_{26}x^2 + 2a_{27}xy + a_{28}y^2) \\
& + \frac{1}{2}\mathbb{C}_{ij21}(a_{17}x^2 + 2a_{18}xy + 3a_{19}y^2 + 3a_{26}x^2 + 2a_{27}xy + a_{28}y^2) \\
& + \mathbb{C}_{ij22}(a_{27}x^2 + 2a_{28}xy + 3a_{29}y^2).
\end{aligned}
\tag{A.2}
$$

Substitution of (A.2) into the constraint (48) results in the following conditions:

$$\langle \hat{\Psi}_{I,1}x^2 \rangle_\Omega = -\langle 2\hat{\Psi}_I x \rangle_\Omega + \langle \hat{\Psi}_I x^2 n_1 \rangle_{\partial\Omega} \quad \forall I \tag{A.3a}$$

$$\langle \hat{\Psi}_{I,2}x^2 \rangle_\Omega = \langle \hat{\Psi}_I x^2 n_2 \rangle_{\partial\Omega} \quad \forall I \tag{A.3b}$$

$$\langle \hat{\Psi}_{I,1}xy \rangle_\Omega = -\langle \hat{\Psi}_I y \rangle_\Omega + \langle \hat{\Psi}_I xy n_1 \rangle_{\partial\Omega} \quad \forall I \tag{A.3c}$$

$$\langle \hat{\Psi}_{I,2}xy \rangle_\Omega = -\langle \hat{\Psi}_I x \rangle_\Omega + \langle \hat{\Psi}_I xy n_2 \rangle_{\partial\Omega} \quad \forall I \tag{A.3d}$$

$$\langle \hat{\Psi}_{I,1}y^2 \rangle_\Omega = \langle \hat{\Psi}_I y^2 n_1 \rangle_{\partial\Omega} \quad \forall I \tag{A.3e}$$

$$\langle \hat{\Psi}_{I,2}y^2 \rangle_\Omega = -\langle 2\hat{\Psi}_I y \rangle_\Omega + \langle \hat{\Psi}_I y^2 n_2 \rangle_{\partial\Omega} \quad \forall I. \tag{A.3f}$$

REFERENCES

1. Chen JS, Pan C, Roque CMOL, Wang HP. A Lagrangian reproducing kernel particle method for metal forming analysis. *Computational Mechanics* 1998; **22**:289–307.
2. Belytschko T, Tabbara M. Dynamic fracture using element-free Galerkin methods. *International Journal for Numerical Methods in Engineering* 1996; **39**:923–938.
3. Moës N, Dolbow J, Belytschko T. A finite element method for crack growth without remeshing. *International Journal for Numerical Methods in Engineering* 1999; **46**:131–150.
4. Guan PC, Chi SW, Chen JS, Slawson TR, Roth MJ. Semi-Lagrangian reproducing kernel particle method for fragment-impact problems. *International Journal of Impact Engineering* 2011; **38**:1033–1047.
5. Guan PC, Chen JS, Wu Y, Teng H, Gaidos J, Hofstetter K, Alsaleh M. Semi-Lagrangian reproducing kernel formulation and application to modeling earth moving operations. *Mechanics of Materials* 2009; **41**:670–683.
6. Nayroles B, Touzot G, Villon P. Generalizing the finite element method: diffuse approximation and diffuse elements. *Computational Mechanics* 1992; **10**:307–318.

7. Belytschko T, Lu YY, Gu L. Element-free Galerkin methods. *International Journal for Numerical Methods in Engineering* 1994; **37**:229–256.
8. Dolbow J, Belytschko T. Numerical integration of the Galerkin weak form in meshfree methods. *Computational Mechanics* 1999; **23**:219–230.
9. Atluri SN, Zhu T. A new meshless local Petrov–Galerkin (MLPG) approach in computational mechanics. *Computational Mechanics* 1998; **22**:117–127.
10. De S, Bathe KJ. The method of finite spheres. *Computational Mechanics* 2000; **25**:329–345.
11. De S, Bathe KJ. The method of finite spheres with improved numerical integration. *Computers and Structures* 2001; **79**:2183–2196.
12. Liu Y, Belytschko T. A new support integration scheme for the weakform in mesh-free methods. *International Journal for Numerical Methods in Engineering* 2010; **82**:699–715.
13. Carpinteri A, Ferro G, Ventura G. The partition of unity quadrature in meshless methods. *International Journal for Numerical Methods in Engineering* 2002; **54**:987–1006.
14. Duflot M, Nguyen-Dang H. A truly meshless Galerkin method based on a moving least squares quadrature. *Communications in Numerical Methods in Engineering* 2002; **18**:441–449.
15. Beissel S, Belytschko T. Nodal integration of the element-free Galerkin method. *Communications in Numerical Methods in Engineering* 1996; **139**:49–74.
16. Chen JS, Wu CT, Yoon S, You Y. A stabilized conforming nodal integration for Galerkin mesh-free methods. *International Journal for Numerical Methods in Engineering* 2001; **50**:435–466.
17. Puso MA, Chen JS, Zywicz E, Elmer W. Meshfree and finite element nodal integration methods. *International Journal for Numerical Methods in Engineering* 2008; **74**:416–446.
18. Chen JS, Hu W, Puso MA, Wu Y, Zhang X. Strain smoothing for stabilization and regularization of Galerkin meshfree methods. In *Meshfree Methods for Partial Differential Equations III*, Griebel M, Schweitzer MA (eds). Springer: Berlin, 2007; 57–75.
19. Liu GR, Dai KY, Nguyen TT. A smoothed finite element method for mechanics problems. *Computational Mechanics* 2007; **39**:859–877.
20. Dyka CT, Randles PW, Ingel RP. Stress points for tension instability in SPH. *International Journal for Numerical Methods in Engineering* 1997; **40**:2325–2341.
21. Krongauz Y, Belytschko T. Consistent pseudo-derivatives in meshless methods. *Computer Methods in Applied Mechanics and Engineering* 1997; **146**:371–386.
22. Bonet J, Kulasegaram S. Correction and stabilization of smooth particle hydrodynamics methods with applications in metal forming simulations. *International Journal for Numerical Methods in Engineering* 2000; **47**:1189–1214.
23. Wang D, Chen JS. Locking-free stabilized conforming nodal integration for meshfree Mindlin-Reissner plate formulation. *Computer Methods in Applied Mechanics and Engineering* 2004; **193**:1065–1083.
24. Chen JS, Wang D. A constrained reproducing kernel particle formulation for shear deformable shell in Cartesian coordinates. *International Journal for Numerical Methods in Engineering* 2006; **68**:151–172.
25. Wang D, Chen JS. A Hermite reproducing kernel approximation for thin-plate analysis with sub-domain stabilized conforming integration. *International Journal for Numerical Methods in Engineering* 2008; **74**:368–390.
26. Duan Q, Li X, Zhang H, Belytschko T. Second-order accurate derivatives and integration schemes for meshfree methods. *International Journal for Numerical Methods in Engineering* 2012; **92**:399–424.
27. Babuška I, Banerjee U, Osborn JE, Li Q. Quadrature for meshless methods. *International Journal for Numerical Methods in Engineering* 2008; **76**:1434–1470.
28. Babuška I, Banerjee U, Osborn JE, Zhang Q. Effect of numerical integration on meshless methods. *Computer Methods in Applied Mechanics and Engineering* 2009; **198**:2886–2897.
29. Liu WK, Jun S, Zhang YF. Reproducing kernel particle methods. *International Journal for Numerical Methods in Fluids* 1995; **20**:1081–1106.
30. Chen JS, Pan C, Wu CT, Liu WK. Reproducing kernel particle methods for large deformation analysis of non-linear structures. *Computer Methods in Applied Mechanics and Engineering* 1996; **139**:195–227.
31. Chen JS, Yoon S, Wu CT. Non-linear version of stabilized conforming nodal integration for Galerkin mesh-free methods. *International Journal for Numerical Methods in Engineering* 2002; **53**:2587–2615.
32. Yoo JW, Moran B, Chen JS. Stabilized conforming nodal integration in the natural-element method. *International Journal for Numerical Methods in Engineering* 2004; **60**:861–890.
33. Lu YY, Belytschko T, Gu L. A new implementation of the element free Galerkin method. *Computer Methods in Applied Mechanics and Engineering* 1994; **113**:397–414.